Two-dimensional particle-in-cell simulations of magnetosonic waves in the dipole magnetic field: On a constant L-shell

Kyungguk Min[1], Kaijun Liu[2], Richard E. Denton[3], František Němec[4], Scott A. Boardsen[5,6], Yoshizumi Miyoshi[7]

[1]Department of Astronomy and Space Science, Chungnam National University, Daejeon, Korea.
[2]Department of Earth and Space Sciences, Southern University of Science and Technology, Shenzhen, China.
[3]Department of Physics and Astronomy, Dartmouth College, Hanover, New Hampshire, USA.
[4]Faculty of Mathematics and Physics, Charles University, Prague, Czech Republic.
[5]NASA/GSFC, Greenbelt, Maryland, USA.
[6]Goddard Planetary Heliophysics Institute, University of Maryland, Baltimore County, Maryland, USA.
[7]ISEE, Nagoya University, Nagoya, Japan.

Key Points:

- 2D PIC simulations are carried out on a constant L-shell surface to simulate the excitation of MSWs for the first time
- Despite the extended unstable region in latitude, MSWs do not grow well if they get latitudinally out of resonance
- Scattering of ring-like protons during MSW excitation is local so that those protons do not necessarily follow Liouville's theorem

Corresponding author: Kyungguk Min, kyungguk@me.com

Abstract

Two-dimensional particle-in-cell (PIC) simulations are carried out on a constant L-shell (or drift shell) surface of the dipole magnetic field to investigate the generation process of near-equatorial fast magnetosonic waves (a.k.a equatorial noise; MSWs hereafter) in the inner magnetosphere. Unlike the simulation domain in a meridional plane used in a recent study, the present simulation box allows wave propagation and growth in the azimuthal direction, to which MSWs were shown to propagate and grow in the source region. Furthermore, the equatorial ring-like proton distribution used to drive MSWs in the present study is (realistically) weakly anisotropic. Consequently, the ring-like velocity distribution projected along the field line by Liouville's theorem extends to rather high latitude, and linear instability analysis using the local plasma conditions predicts substantial MSW growth up to $\pm 27^\circ$ latitude. In the PIC simulations, however, the MSW intensity maximizes near the equator and decreases quasi-exponentially with latitude. Further analysis reveals that the stronger equatorward refraction at higher latitude due to the larger gradient of the dipole magnetic field strength prevents off-equatorial MSWs from growing continuously, whereas MSWs of equatorial origin experience little refraction and can fully grow. Furthermore, the simulated MSWs exhibit a rather complex wave field structure varying with latitude, and the scattering of energetic ring-like protons in response to MSW excitation occurs faster than the bounce period of those protons so that they do not necessarily follow Liouville's theorem during MSW excitation.

1 Introduction

Near-equatorial fast magnetosonic waves (MSWs hereinafter) are among the most frequently observed plasma waves in the inner magnetosphere (radial distances $\lesssim 10\,R_E$, where R_E is Earth radius) and have the largest amplitude in the frequency band between a few Hz and ~ 100 Hz (Santolík et al., 2004; Meredith et al., 2008; Ma et al., 2013; Hrbáčková et al., 2015; Posch et al., 2015; Boardsen et al., 2016). MSWs are also referred to as equatorial noise after the initial discovery by Russell et al. (1970). Soon after, it was found that the noise-like emissions near the equator can be described as the oblique whistler mode or the high-frequency extension of the fast magnetosonic mode in a proton-electron plasma (Boardsen et al., 1992; Němec et al., 2006; Walker et al., 2015; Boardsen et al., 2016). The defining characteristic of MSWs includes a series of spectral peaks at or near harmonics of the proton cyclotron frequency, $f_{\rm cp}$, between $f_{\rm cp}$ and the lower hybrid frequency; high magnetic compressibility, $|\delta B_\parallel|^2 \gg |\delta B|^2$ (e.g., Perraut et al., 1982; Boardsen et al., 1992; Santolík et al., 2004; Boardsen et al., 2016); and propagation quasi-perpendicular to the background magnetic field. (Throughout the paper, subscripts $\parallel$ and $\perp$ indicate the directions parallel and perpendicular to the background magnetic field, respectively.) Also, according to the cold plasma magnetosonic mode dispersion relation, the longitudinal component of the wave electric field is much greater than the transverse component for frequencies greater than about $3f_{\rm cp}$ (see, e.g., Boardsen et al., 2016, Figure 1); this has been used to experimentally determine the equatorial propagation direction of MSWs (Santolík et al., 2002; Němec et al., 2013; Boardsen et al., 2018). The generation of MSWs most likely involves proton cyclotron resonant interactions with energetic protons having a ring-like velocity distribution with a positive slope in the perpendicular velocity direction, $\partial f/\partial v_\perp > 0$ (Gulelmi et al., 1975; Gurnett, 1976; Perraut et al., 1982; Boardsen et al., 1992; Horne et al., 2000; Chen et al., 2010; Liu et al., 2011).

Observations (Gurnett, 1976; Perraut et al., 1982; Laakso et al., 1990; Kasahara et al., 1994; André et al., 2002; Santolík et al., 2004; Němec et al., 2005; Němec et al., 2006; Němec et al., 2015; Hrbáčková et al., 2015; Boardsen et al., 2016; Yuan et al., 2019; Zou et al., 2019) have shown that MSWs occur most frequently within 10° latitude from the magnetic equator and their amplitudes likewise exhibit a narrow latitudinal extent with a peak at the magnetic equator. Based on ray tracing analyses, it has long been

suggested that wave sources are similarly located near the magnetic equator (e.g., Boardsen et al., 1992; Horne et al., 2000; Shklyar & Balikhin, 2017). MSWs generated from an equatorial source region with a wave normal angle, $\theta_{\mathbf{k}}$, deviating from 90° can propagate away from the source region toward higher latitudes. As they propagate, their $\theta_{\mathbf{k}}$ approaches 90° due to refraction, and the waves are eventually reflected back toward equator (Boardsen et al., 1992, Figures 5 and 8). Due to the quasi-perpendicular propagation, most of the MSWs generated at an equatorial source region will remain close to the magnetic equator. Furthermore, the MSWs that are reflected at high latitude experience a shorter duration of wave growth (or a longer duration of damping) than the waves that remain at the equator, hence explaining the observed amplitude peak at the equator. This is because the largest wave growth occurs close to harmonics of the local f_{cp} and close to $\theta_{\mathbf{k}} = 90°$ (e.g., Boardsen et al., 1992; Chen, 2015). Boardsen et al. (1992, 2016) argued that the harmonic-dependent reflection latitude can account for the frequently observed, funnel-shaped features in frequency-time spectrograms: For similar equatorial $\theta_{\mathbf{k}}$, lower-frequency MSWs are more closely confined to the magnetic equator than higher-frequency MSWs; and for similar reflection latitude, lower-frequency MSWs experience stronger damping while passing through the same equatorial region (Boardsen et al., 1992, Figure 9); however, a follow-up study using gain analysis was not performed. Zhima et al. (2015) analyzed MSWs that were observed at about −17° latitude and which exhibited discrete spectral peaks with frequency spacing of adjacent spectral lines not equal to the local f_{cp}. Using backward ray tracing, they suggested that propagation from spatially narrow equatorial source regions can account for the observed discrete spectral structures.

In recent years, much attention has been paid to the spatial distribution of MSWs and their dispersion properties (e.g., Zou et al., 2019; Ma et al., 2019) because of the potential role that they play in accelerating and scattering radiation belt electrons. It has been demonstrated that radiation belt electrons can interact with MSWs through Landau resonance (Horne et al., 2007), transit-time scattering (Bortnik & Thorne, 2010), and bounce resonance (Chen et al., 2015; Li et al., 2015). Horne et al. (2007) was the first to suggest that electron acceleration can occur via Landau resonance with scattering rates comparable to those for whistler mode chorus. Bortnik and Thorne (2010) demonstrated that the lack of parallel wave field structure (due to quasi-perpendicular propagation) and the equatorial confinement of MSWs can cause a new type of scattering effect called the transit-time effect. They suggested that Landau resonance with electrons is only effective near the equator where average $\theta_{\mathbf{k}}$ of MSWs becomes minimum (according to the equator-wave-source mechanism), whereas transit-time scattering is able to scatter electrons over the entire latitudinal extent of the waves. On the other hand, bounce resonance with MSWs can be particularly important for the scattering of near-equatorially-mirroring electrons (Roberts & Schulz, 1968; Shprits, 2009). Considering that MSWs are generated near the equator and propagate away from it, Tao and Li (2016) and Li and Tao (2018) showed that the bounce resonance is sensitive to the $\theta_{\mathbf{k}}$ distribution and the latitudinal extent of wave power. Furthermore, the bounce diffusion rate can be comparable to the diffusion rate caused by Landau resonance.

Self-consistent particle-in-cell (PIC) simulations of plasma waves in the inner magnetosphere are useful not only to understand the generation process of waves but to quantify their effect on energetic electrons in the Van Allen belts. Moreover, they can complement the limitations of observations that have to contend with the limited spatiotemporal coverage, measurement quality, and limited high-resolution datasets. Unlike electromagnetic ion cyclotron (EMIC) waves and whistler-mode chorus (e.g., Denton et al., 2014; Denton, 2018; Lu et al., 2019), however, self-consistent simulations of MSWs have until recently been limited to homogeneous plasmas in a uniform background magnetic field. Chen et al. (2018) carried out two-dimensional simulations of MSWs in a meridional plane of a scaled-down dipole magnetic field for the first time, and were able to test the equator-wave-source mechanism mentioned above. In their model, the free energy

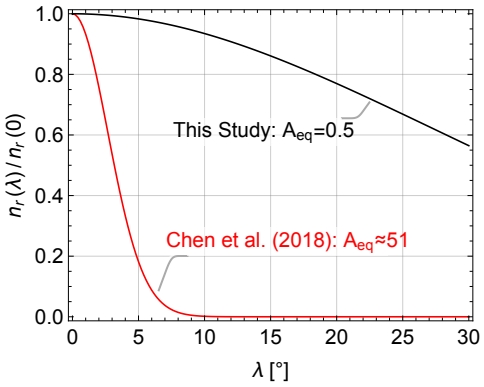

Figure 1. Comparison between the energetic proton ring density used in Chen et al. (2018) (red) and the partial shell density in this study (black), plotted versus latitude. Equivalent equatorial temperature anisotropies (A_{eq}) are 51 and 0.5, respectively.

source (i.e., energetic ring protons) was limited to well within ±10° latitude (see Figure 1; red curve) and also in L-shell. According to their results, MSWs excited in that equatorial source region were confined to the equator. Interestingly, the waves in their simulation propagated in the radial direction with wave normal directions nearly perpendicular to the background magnetic field. They noted that the lack of wave structure along the field line indicates the importance of the transit-time effect over Landau resonance. On the other hand, Min, Boardsen, et al. (2018) and Min et al. (2019) carried out two-dimensional PIC simulations of MSWs on the equatorial plane of the dipole magnetic field, focusing on the equatorial evolution with and without the steep density gradient of the plasmapause.

The present study investigates the generation process of MSWs using two-dimensional PIC simulations. The major difference from Chen et al. (2018) is that the simulation domain is contained in a constant L-shell surface instead of the meridional plane. This is to take into account the observational fact that the dominant MSW propagation is along the azimuthal direction in the source region (Němec et al., 2013; Boardsen et al., 2018). Section 2 outlines the motivation and goal of the present simulation study. Section 3 describes the simulation setup, and section 4 presents the simulation results. Section 5 further discusses the simulation results and section 6 concludes the paper. To keep the paper brief, non-essential materials including some considerations for the modeling approach are presented through supporting information.

2 Motivation and Goal

Although Chen et al. (2018)'s simulations demonstrated the MSW excitation and propagation consistent with the equator-wave-source mechanism, we find that some assumptions in their model and some of their simulation results do not have strong observational support.

First, in order to limit the free energy source into a narrow latitudinal region, Chen et al. (2018) had to use an equatorial temperature anisotropy of the proton ring distribution equivalent to $A_{eq} \equiv T_{\perp,eq}/T_{\parallel,eq} - 1 \approx 51$ (where $T_{\parallel}$ and $T_{\perp}$ are the effective temperatures parallel and perpendicular to the background magnetic field, respectively, and the subscript "eq" denotes that the quantities involved are the equatorial values). According to Liouville's theorem, the number density of a plasma population having a pancake distribution at the equator decreases with increasing latitude (via dependence

on the magnetic field strength), and the more anisotropic the pancake distribution is, the faster the ring/shell density decreases with latitude (e.g., Roederer, 1970). Figure 1 shows in red the number density as a function of latitude for the proton ring distribution used in Chen et al. (2018). Although not impossible, such a large value of equatorial anisotropy is improbable for typical inner magnetospheric conditions (e.g., Thomsen et al., 2017). In addition, temperature anisotropy of that magnitude can lead to the excitation of strong EMIC waves (e.g., Min et al., 2016), although their simulations do not appear to show parallel-propagating EMIC waves within the time period of their simulation run. Apparently, one would want to test the generation process using the conditions more commonly found in the inner magnetosphere. In fact, we use a value of equatorial temperature anisotropy, $A_{\rm eq} = 0.5$ based on the event analysis of Min, Liu, Wang, et al. (2018), which lies at the bottom end of the anisotropy range surveyed by Thomsen et al. (2017). As shown in Figure 1, the decrease of the energetic proton ring density is much more gradual with this more realistic anisotropy value and there still exist a substantial fraction (60%) of energetic ring protons at 30° latitude. According to the complementing linear analysis and kinetic simulations of Min and Liu (2020) using the local plasma conditions along the field line, the saturation amplitudes of excited MSWs monotonically decrease with latitude, although the initial growth rate maximizes away from the equator (at around 20° latitude). This suggests that we may still achieve the observed latitudinal wave confinement even with a wide latitudinal extent of the free energy source. (That is, a limited wave source region may not be necessary to produce latitudinally limited MSWs.)

Second, recent observational studies (Němec et al., 2013; Boardsen et al., 2018) showed that propagation of MSWs in low density regions (where the conditions are favorable for wave excitation) is dominantly in the azimuthal direction. By simple ray tracing calculation assuming an azimuthally symmetric medium, Boardsen et al. (2018) predicted that optimal wave growth at the source region will occur for waves propagating along the contour of constant magnetic field magnitude (that is, in the azimuthal direction) rather than in the radial direction. This was confirmed by Min, Boardsen, et al. (2018) from two-dimensional PIC simulations of MSWs considering propagation exactly perpendicular to the background magnetic field in the equatorial plane. So, for MSW simulations it seems necessary to allow wave propagation in the azimuthal direction in order to properly model the generation process of MSWs in the source region. In the present study, we choose a two-dimensional simulation domain on a constant L-shell surface in the dipole magnetic field, which ignores the radial dependence of quantities. This is appropriate because in the dipole magnetic field, all particles with the same drift invariant (or L^*) share the same L-shell. On the other hand, the present setup suppresses radial propagation of MSWs (and in fact any fluctuations), even though MSWs are known to naturally refract radially outward (and inwards just inside the plasmapause) (Gulelmi et al., 1975; Chen & Thorne, 2012).

The last point concerns the lack of parallel wave structure in the simulation results of Chen et al. (2018): MSWs excited in their simulations exhibited nearly field-aligned wave fronts at all latitudes. This seems counterintuitive, because the ray tracing analyses (e.g., Boardsen et al., 1992; Horne et al., 2000) show a varying wave normal angle as a wave packet propagates along and across the field line. In addition, recent statistical analysis by Zou et al. (2019) seems to indicate the change in the wave normal angle with latitude such that the average $\theta_{\mathbf{k}}$ is relatively narrowly peaked about 90° near the equator and decreases monotonically with latitude, although we should note that they presented no concrete analysis to show and understand the impact of the error in individual $\theta_{\mathbf{k}}$ measurements (see section 5). The discrepancy, or lack thereof, further motivates us to explore more realistic assumptions.

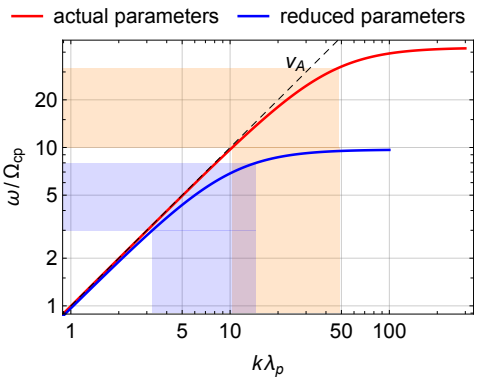

Figure 2. Comparison between the cold plasma dispersion relations for the actual (red) and reduced (blue) parameters (for $\theta_{\mathbf{k}} = 90^\circ$). The light orange and blue shaded areas respectively denote the approximate frequency range of observed MSWs and the range where MSWs are excited in the present simulations.

3 Simulation Setup

3.1 Key Plasma Parameters

The initial simulation parameters used in the present study are based on those of our earlier simulations (Min, Liu, Denton, & Boardsen, 2018; Min, Boardsen, et al., 2018), which were derived from the actual MSW event studied in detail by Min, Liu, Wang, et al. (2018) and Boardsen et al. (2018). The key observational parameters for the event are: The equatorial radial distance is ∼5.6 R_E, the equatorial (total) plasma number density is $n_{e,\mathrm{eq}} \approx 24$ cm^{-3}, and the equatorial magnetic field strength is $B_{\mathrm{eq}} \approx 131$ nT. The corresponding electron plasma-to-cyclotron frequency ratio is $\omega_{pe,\mathrm{eq}}/\Omega_{ce,\mathrm{eq}} \approx 12$, and the light-to-Alfvén speed ratio is $c/v_{A,\mathrm{eq}} \approx 514$, where $\omega_{pe,\mathrm{eq}} = \sqrt{4\pi n_{e,\mathrm{eq}} e^2/m_e}$; $\Omega_{ce,\mathrm{eq}} = eB_{\mathrm{eq}}/(m_e c)$; and $v_{A,\mathrm{eq}} = B_{\mathrm{eq}}/\sqrt{4\pi m_p n_{e,\mathrm{eq}}}$. The Alfvén energy is $E_{A,\mathrm{eq}} \equiv m_p v_{A,\mathrm{eq}}^2/2 \approx 1.78$ keV. The subscript "eq" indicates that the quantity under consideration is an equatorial value.

Since we desire to carry out simulations in a box in proportion to the actual scale (assuming that the dipole field is a reasonable approximation to the Earth's magnetic field at $L \sim 5.6$), our simulation domain is accordingly placed at the dipole L value of 5.6. (In terms of the proton inertial length, $\lambda_{p,\mathrm{eq}} \equiv c/\omega_{pp,\mathrm{eq}} = v_{A,\mathrm{eq}}/\Omega_{cp,\mathrm{eq}}$, to which MSWs are scaled, $L = 770\lambda_{p,\mathrm{eq}}/R_E$.)

Due to the limited computational resources available, we use a reduced value for $c/v_{A,\mathrm{eq}} = 40$, which increases our simulation time step (Δt) drastically. For fixed $n_{e,\mathrm{eq}}$, this is equivalent to the Earth's dipole magnetic moment being one hundred times larger than the actual value. However, it is important to point out that the relative field line geometry is unchanged. In addition to the reduced $c/v_{A,\mathrm{eq}}$, we utilize a reduced value for the proton-to-electron mass ratio $m_p/m_e = 100$ to alleviate the scale difference between electrons and ions. This leads to $\omega_{pe,\mathrm{eq}}/\Omega_{ce,\mathrm{eq}} = (c/v_{A,\mathrm{eq}})\sqrt{m_e/m_p} = 4$ in our simulations (that is, we consider much heavier electrons).

Figure 2 shows a comparison between the cold plasma dispersion relations for $\theta_{\mathbf{k}} = 90^\circ$ for the actual and reduced parameters. Note that while the proton inertial length (to which the wavelength is scaled) is identical in both cases, the proton cyclotron frequency (to which the wave frequency is scaled) is about thirteen times larger for the reduced parameters because of the increased dipole moment. The light orange region de-

notes the frequency range of the MSW event studied in Min, Liu, Wang, et al. (2018). (It is also worth pointing out that statistically, wave power in the plasma trough is typically concentrated above 10th harmonic (Boardsen et al., 2016; Němec et al., 2015).) For the present parameters which will be described shortly, our simulations cover the lower end of the full MSW spectrum (Min & Liu, 2020), and longer wavelength modes.

3.2 Initial Plasma Distribution

MSWs derive their energy from energetic protons having a ring-like velocity distribution with $\partial f/\partial v_\perp > 0$. There are several widely-used, analytical distribution functions of this kind (e.g., Horne et al., 2000; Liu et al., 2011; Chen et al., 2018). Here, consistent with our previous studies (Min, Liu, Wang, et al., 2018; Min, Liu, Denton, & Boardsen, 2018; Min, Boardsen, et al., 2018; Min et al., 2019), we use the partial shell velocity distribution given by

$$f_{s,\mathrm{eq}}(v,\alpha) = \frac{n_{s,\mathrm{eq}}}{\pi^{3/2}\theta_s^3 C(v_s/\theta_s)} \exp\left(-\frac{(v-v_s)^2}{\theta_s^2}\right) \sin^{2A}\alpha, \tag{1}$$

where $v = |\mathbf{v}|$ is the velocity modulus; α is the pitch angle; A is the effective temperature anisotropy, $A = T_\perp/T_\parallel - 1$; v_s and θ_s are the ring (or shell) speed and the thermal spread of the shell, respectively; $n_{s,\mathrm{eq}}$ is the number density; and $C(x)$ is the normalization constant given by

$$C(x) = \left[xe^{-x^2} + \sqrt{\pi}\left(\frac{1}{2}+x^2\right)\mathrm{erfc}(-x)\right]\frac{\Gamma(1+A)}{\Gamma(3/2+A)}. \tag{2}$$

The subscript "eq" is to remind the readers that this partial shell distribution is described at the equator. Since according to Liouville's theorem the distribution function is constant along the trajectory of representative particles, one can obtain the particle distributions anywhere along the field line (e.g., Roederer, 1970). Making use of the conservation of particle kinetic energy, $KE = mv^2/2$, and the magnetic moment, $\mathcal{M} = mv_\perp^2/(2B)$, one may get the velocity distribution mapped to latitude λ_{lat} (Xiao & Feng, 2006)

$$f_s(\lambda_{\mathrm{lat}}; v, \alpha) = \frac{n_s(\lambda_{\mathrm{lat}})}{\pi^{3/2}\theta_s^3 C(v_s/\theta_s)} \exp\left(-\frac{(v-v_s)^2}{\theta_s^2}\right) \sin^{2A}\alpha, \tag{3}$$

where we have defined the partial shell density n_s as

$$n_s(\lambda_{\mathrm{lat}}) = n_{s,\mathrm{eq}}\left(\frac{B_{\mathrm{eq}}}{B(\lambda_{\mathrm{lat}})}\right)^A. \tag{4}$$

Consequently, only the number density, but not the shape of the velocity distribution function, is dependent upon the field line coordinate. Here, $B(\lambda_{\mathrm{lat}}) = B_{\mathrm{eq}}\sqrt{1+3\sin^2\lambda_{\mathrm{lat}}}/\cos^6\lambda_{\mathrm{lat}}$ for the dipole magnetic field. The isotropic Maxwellian velocity distribution is recovered when $v_s = 0$ and $A = 0$, for which the number density becomes constant along the field line.

For simplicity, we consider a three-component plasma consisting of a tenuous partial shell proton population (denoted by subscript s), a dense isotropic background proton population (denoted by subscript p), and a charge-neutralizing isotropic electron population (denoted by subscript e). In the present simulations, $n_{s,\mathrm{eq}}/n_e = 0.025$, $v_s = 1.7v_{A,\mathrm{eq}}$, $\theta_s = 0.43v_{A,\mathrm{eq}}$, and $A = 0.5$. Compared to our previous simulation studies, n_s is reduced by half in order to delay the growth time scale of MSWs. In addition, the background proton and electron populations are assumed to be cold and their dynamics is accordingly solved using the cold fluid approach (Tao, 2014). There are two reasons for this hybrid approach. First, it helps reduce the computational cost and discrete particle noise. Particularly, test simulations show that the background noise level is strongly dependent on latitude (a larger noise level at higher latitude) when the background populations are also treated kinetically. It turns out that keeping the noise level low at high

latitude is very important because the wave amplitudes there are low. Second, it has been noticed that a parallel-propagating secondary mode develops in simulations when the background populations are also treated kinetically. This mode also appeared in simulations of Min and Liu (2016) (see, e.g., Figure 7 therein), but we did not investigate its cause at that time. After some tests, we concluded that this mode is unlikely driven by the initially anisotropic partial shell distribution or the anisotropic background proton population at the later stage of simulation as a result of perpendicular heating. Rather, it appears that some nonlinear effect involving the excited MSWs and the thermal background populations plays a role. Without a clear resolution at the moment and also due to the noise concern, we decided to forgo the kinetic treatment of the background populations and instead revisit this issue in a future study. On the other hand, the main role of the background populations is, insofar as the present study is concerned, to support wave propagation. So, using the hybrid approach, we take the kinetic effect of the background populations out of the picture and focus on the kinetic physics driven by the energetic partial shell protons. (For reference, the response of background populations were discussed in Chen et al. (2018), Sun et al. (2017), and references therein.) Min and Liu (2020) provides an extensive comparison between the linear theory analysis and simulations using local plasma conditions at various latitudes, providing the validity and justification of our hybrid approach.

Before moving forward, we compare the present simulation parameters to Chen et al. (2018)'s. Similar to our simulation parameters, Chen et al. (2018) used reduced values for $m_p/m_e = 100$ and $c/v_{A,\mathrm{eq}} = 20$. The center of their simulation domain, however, was located at $L = 1$ (thus using the field line geometry at that location). They also used a three-component electron-proton plasma including a charge-neutralizing electron population. The background proton and electron populations had a Maxwellian velocity distribution with temperature equivalent to 1 eV. For the energetic proton population that drives MSWs, they used a Maxwellian-ring velocity distribution (see Chen et al., 2018, Eq. (2)) with a 5% concentration, ring speed $V_R = v_{A,\mathrm{eq}}$, and the thermal spread of the ring $w_{\mathrm{pr}} = 0.141 v_{A,\mathrm{eq}}$ at the center of the simulation domain. The maximum temperature anisotropy at the center was $A_{\mathrm{eq}} \approx 51$, resulting in the free energy source contained well within $\pm 10°$ latitude (see Figure 1). Despite the small (5%) concentration of the ring protons, the combination of the large A_{eq} and the small thermal spread of the ring yielded a large maximum growth rate of about $0.5\Omega_{cp,\mathrm{eq}}$ at the center of the simulation domain.

3.3 Simulation Domain

Having determined the base parameters, we now describe the rest of the simulation parameters.

Figures 3a–3b display the latitudinal dependence of some key parameters. The dipole magnetic field $B(\lambda_{\mathrm{lat}})$ is almost three times larger at 30° latitude than B_{eq}. The Alfvén speed profile $v_A(\lambda_{\mathrm{lat}})$ closely follow $B(\lambda_{\mathrm{lat}})$, because partial shell protons (2.5% at most) does not contribute significantly to the proton mass density. (Also, this means that the proton inertial length is only weakly dependent on latitude, $\lambda_p(\lambda_{\mathrm{lat}}) \approx \lambda_{p,\mathrm{eq}}$.) Since the absolute value for v_s is constant, the ratio v_s/v_A, which determines the unstable harmonic frequency range of MSWs, is inversely proportional to v_A. This value drops below 0.7 at about 26° latitude and above (see Min & Liu, 2020). The ratio of the lower hybrid frequency, $\omega_{lh}(\lambda_{\mathrm{lat}})$, to the local proton cyclotron frequency, $\Omega_{cp}(\lambda_{\mathrm{lat}})$, on the other hand, is related to the highest MSW harmonic mode that the system allows. This ratio (given by $\omega_{lh}/\Omega_{cp} = 1/\sqrt{v_A^2/c^2 + m_e/m_p}$) starts from just below 10 at the equator and monotonically decreases with increasing latitude. Up until 29° latitude, there can be at least eight harmonic modes. The transition of ω_{lh}/Ω_{cp} from above 9 to below is marked with the vertical dashed line in Figure 3b drawn at 22.5° latitude. The simulated wave energy exhibits a sudden drop around this latitude (next section). Figure 3c shows the lin-

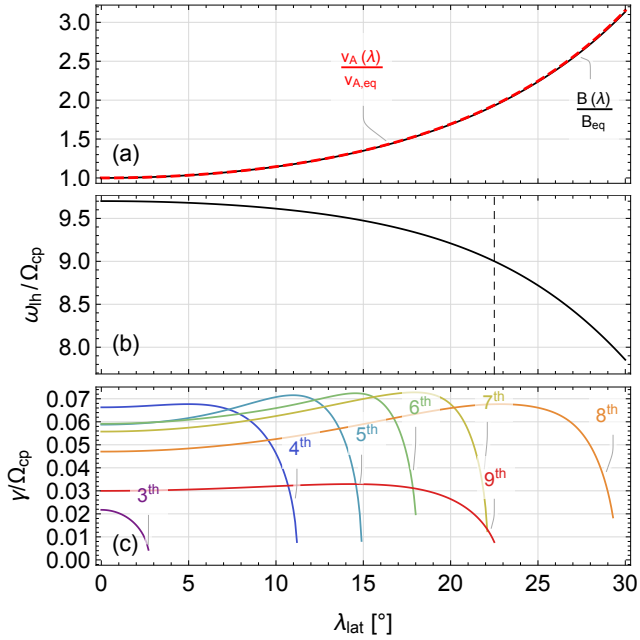

Figure 3. Latitudinal dependence of (a) the dipole magnetic field strength, B (black), and the Alfvén speed, v_A (red); and (b) the ratio of the lower hybrid frequency, ω_{lh}, to the local proton cyclotron frequency, Ω_{cp}. (c) Maximum growth rates (normalized by Ω_{cp}) at $\theta_{\mathbf{k}} = 90°$ versus latitude. Colors correspond to the different harmonics as labeled.

ear growth rates at $\theta_{\mathbf{k}} = 90°$ calculated using the approximate formula given by Gulelmi et al. (1975). Note that the growth rate, γ, is normalized by Ω_{cp}. Because the maximum value of γ/Ω_{cp} over all harmonics is ~ 0.07 up to about 27° latitude and Ω_{cp} increases with latitude, MSWs actually grow fastest initially near 25° latitude (Min & Liu, 2020, Figure 1).

Based on the above analysis, using latitudinal boundaries at about ±30° latitude should be sufficient. Figure 4a displays a three-dimensional rendering of the simulation box (red outline). We set the simulation grid sizes at the equator as $r_0\Delta\phi\times\Delta s = 0.05\lambda_p\times 0.5\lambda_p$, where ϕ is the azimuthal coordinate, $\mathrm{d}s = r_0\cos\lambda_{\rm lat}\sqrt{4-3\cos^2\lambda_{\rm lat}}\,\mathrm{d}\lambda_{\rm lat}$ is the dipole field line arc length, and $r_0 = LR_E$ is the equatorial distance from the Earth center to the field line. The field line grid spacing increases with latitude proportional to $B(\lambda_{\rm lat})$ to keep the flux tube volume roughly constant (Hu & Denton, 2009). The number of the grid points is $N_\phi \times N_{\lambda_{\rm lat}} = 480 \times 1200$. The length of the simulation domain in the azimuthal direction ($N_\phi\Delta\phi = 1.8°$) is sufficient to resolve the longest MSWs. (The simulation box can contain about 20 wave cycles of the 4th harmonic mode in the azimuthal direction.) The simulation time step is $\Delta t = 0.0005\Omega_{cp,\rm eq}^{-1}$. Since the azimuthal extent of the source region is typically much larger than the radial extent, the periodic boundary conditions in the azimuthal direction may be appropriate. In contrast, absorbing boundary conditions are used in the latitudinal boundaries to damp out the outgoing waves (Umeda et al., 2001), although most of MSWs excited in the system are refracted toward the equator before reaching the latitudinal boundaries (section 4). Since the width of each absorbing layer is 20 grid points wide, the physical domain size in the field line direction is actually 1160 grid points wide (or equivalently $\lambda_{\rm lat} \approx \pm 27°$). The number of the simulation particles for the energetic partial shell proton population is on average 2500 per cell.

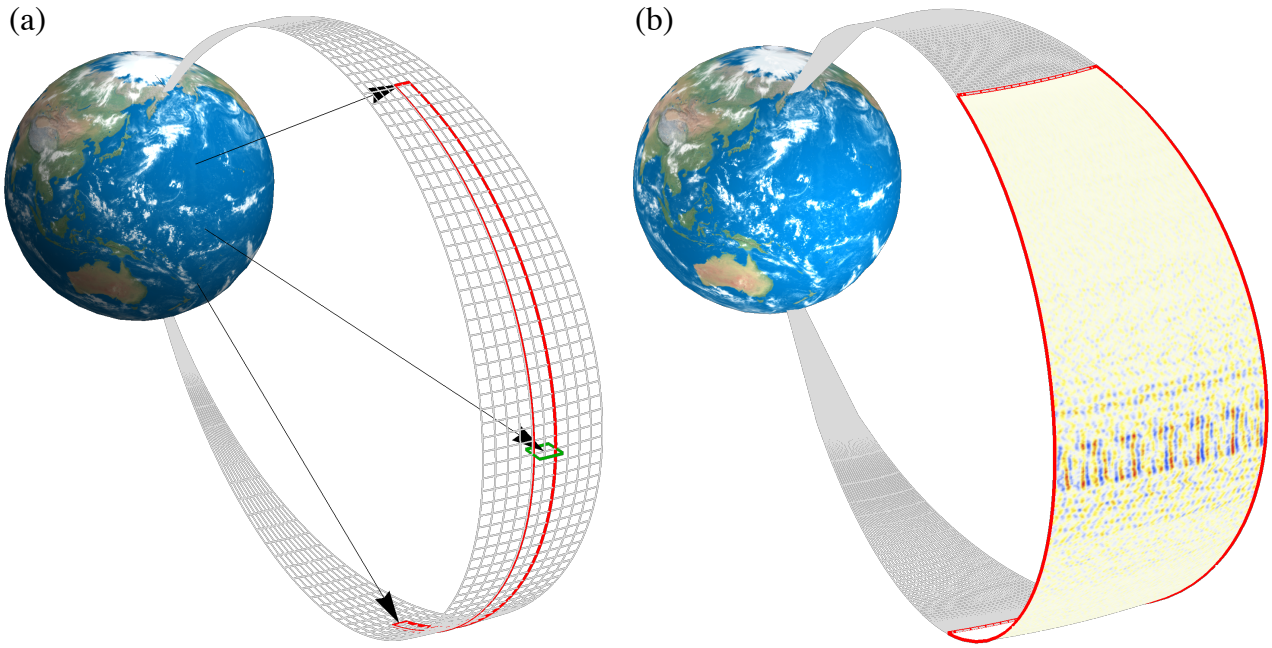

Figure 4. (a) Three-dimensional rendering of the constant L-shell surface (gray mesh) and the outline of the present simulation domain (red). The green box at the equator for comparison denotes the simulation box used in Min, Liu, Denton, and Boardsen (2018). (b) Three-dimensional rendering of the azimuthal component of the simulated electric field, δE_ϕ, at $t\Omega_{cp,\mathrm{eq}} = 130$. The azimuthal dimension has been stretched by a factor of ten to display the wave field structure. (Earth globe texture provided courtesy of Tom Patterson, www.shadedrelief.com.)

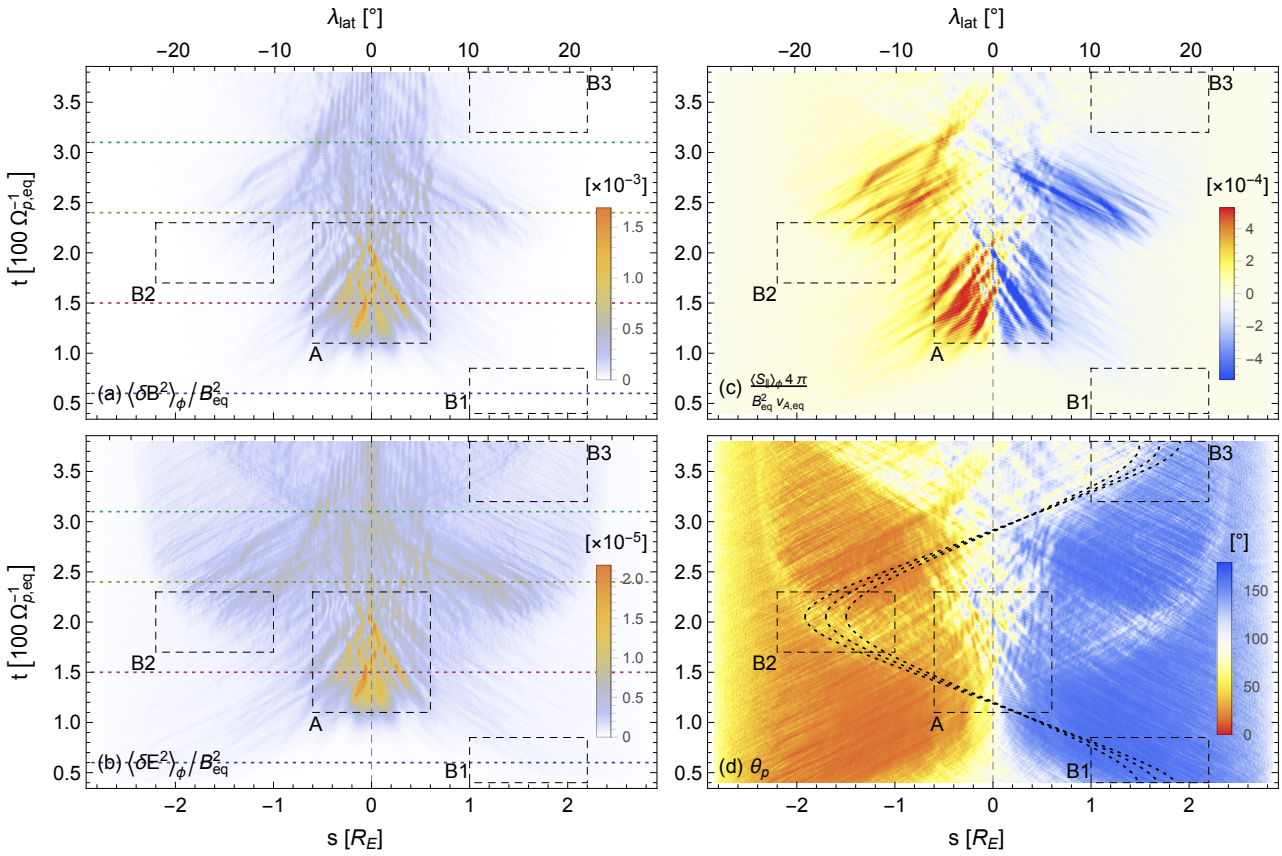

Figure 5. (a–b) Two-dimensional color plots of (a) magnetic, $\langle \delta B^2 \rangle_\phi$, and (b) electric, $\langle \delta E^2 \rangle_\phi$, field intensity as a function of time and field line coordinate (or magnetic latitude). The color scale is linear, and $\langle \cdot \rangle_\phi$ means averaging over the azimuthal grid points. Energy is normalized by $B_{\rm eq}^2$. (c) Parallel component of the Poynting flux, $\langle S_\parallel \rangle_\phi$, as a function of time and field line coordinate (or magnetic latitude). The Poynting flux is normalized by $B_{\rm eq}^2 v_{A,\rm eq}/4\pi$. (d) Poynting vector angle, $\theta_p = \cos^{-1}(\langle S_\parallel \rangle_\phi / \langle |\mathbf{S}| \rangle_\phi)$. The color map is chosen to match that of (c): Reddish and bluish color means Poynting vector directions northward and southward, respectively. The three dotted curves superimposed are the trajectories of sample rays of the 8th harmonic.

4 Simulation Results

Figure 4b displays a three-dimensional rendering of the simulated electric field fluctuations, δE_ϕ, around the time of wave energy saturation (see Figure 5a). (The azimuthal dimension has been stretched by a factor of ten to visualize the azimuthal wave structure.) To effectively convey the main results of the present simulation, we focus on the presentation of latitude-time wave intensity distribution to investigate the global evolution of MSWs; spatial and temporal power spectrograms to investigate wave spectral properties; and the energetic proton distribution function to investigate the evolution of free energy.

4.1 Wave Energy and Poynting Flux

Figures 5a and 5b show fluctuating electric and magnetic field intensity, $\langle \delta E^2 \rangle_\phi$ and $\langle \delta B^2 \rangle_\phi$, as a function of time and field line coordinate, where the angled bracket means

average over the azimuthal grid points, $\langle\cdot\rangle_\phi = \frac{1}{N_\phi}\sum_{i=1}^{N_\phi}$. The upper tick marks indicate magnetic latitude, and the color bar scale is linear. First of all, both the electric field and magnetic field exhibit maximum intensity near the equator around $t\Omega_{cp,\mathrm{eq}} = 150$, indicated by the rectangular box labeled "A". The box spans $\pm 6°$ in latitude, so the wave energy is roughly contained within this range. Before reaching the maximum intensity, the faint streak-like pattern merges toward the equator as if waves have been propagated toward the equator. It is not clear at this point how much the waves excited off the equator contribute to the intensity peak at the equator. One can anticipate that if the waves excited near the equator are the main contributor, the frequency spectrum will exhibit discrete harmonic peaks and the average normal angle will be close to 90° (see Min & Liu, 2020). If, on the other hand, the off-equatorial waves are the main contributor, the average value for $\theta_{\mathbf{k}}$ will become smaller due to the spread in the wave normal angle distribution and the discrete harmonic pattern will be less pronounced due to superposition of MSWs from multiple sources at different latitudes. We will show in the next section that the waves contained in box "A" are mainly from the equatorial source.

After wave intensity has reached the primary maximum around $t\Omega_{cp,\mathrm{eq}} = 150$, there appears a secondary enhancement starting from $t\Omega_{p,\mathrm{eq}} \approx 200$. It extends over a much broader latitudinal range as indicated by the box labeled "B2". Although only one box in the southern hemisphere is drawn, the system is symmetric about the equator and the same process is mirrored to the other hemisphere. This secondary enhancement is more pronounced in $\langle \delta E^2 \rangle_\phi$ due in part to the fact that the wave frequency gets closer to ω_{lh} and MSWs become more electrostatic in nature. In Figure 5b, the streak-like pattern clearly indicates that the waves excited in a wide latitudinal extent subsequently propagate toward the equator and then to the opposite hemispheres. Near the end of the run, the waves that have reached the opposite hemispheres experience a refraction and subsequently propagate toward the equator (refer to the region outlined by the box labeled "B3"; and also Figure S6b).

Based on these observations, we may group the waves in the simulation into two. The first group involves the waves that contribute to the primary intensity maximum at the early stage of the simulation (box "A") and decay afterward. The waves in this group remain near the equatorial region throughout the run (well contained within the latitudinal extent of box "A") and form the standing-wave pattern after $t\Omega_{cp,\mathrm{eq}} \gtrsim 240$. The waves in the second group, in contrast, occupy a larger latitudinal extent (but with lower intensity) and are more dynamic in that they bounce back and forth between two conjugate hemispheres, as often shown in ray tracing studies. It appears that the initial waves excited around box "B1" travel to box "B2" in the opposite hemisphere where they experience refraction and subsequently pick up more energy (or they provide the seed fluctuations for the secondary enhancement), and then bounce back to box "B3". (Note that these wave packets also move in the azimuthal direction, and probably in the radial direction as well in the full three-dimensional case.) By symmetry, the waves starting at the southern hemisphere will go through the same process but in the opposite direction. We will present supporting evidence for this interpretation in the rest of the paper.

Figure 5c shows the parallel component of the Poynting flux averaged over the azimuthal grid points, $\langle S_\parallel \rangle_\phi$. The bluish and reddish colors indicate propagation northward ($S_\parallel > 0$) and southward ($S_\parallel < 0$), respectively. The double-peaked wave intensity structure in time is also shown in $\langle S_\parallel \rangle_\phi$ (one at around $t\Omega_{cp,\mathrm{eq}} = 150$ and the other at around $t\Omega_{cp,\mathrm{eq}} = 250$). More interestingly, the direction of the Poynting vector is dominantly equatorward such that it points northward (southward) at the southern (northern) hemisphere. Nevertheless, the signatures of poleward Poynting flux is sparsely shown. For example, within boxes "A" and "B3" in Figure 5d, wave packets originating from the opposite hemispheres maintain substantial intensity so that they leave the trace of poleward Poynting flux.

Figure 5d shows the angle, θ_p, between the Poynting vector and the dipole magnetic field vector. (Note that θ_p is not the same as the wave normal angle, $\theta_{\mathbf{k}}$.) The color map is reversed to match the directionality of Figure 5c. The main purpose of the θ_p plot is to highlight the trajectories of simulated wave packets. We have calculated sample ray trajectories using the formulae given by Shklyar and Balikhin (2017). Superimposed in Figure 5d are three sample trajectories of the 8th harmonic traced forward and backward in time starting from -19, -17, and $-15°$ latitudes centered at $t\Omega_{cp,\mathrm{eq}} = 210$ (inside box "B2"). All rays initially had $\theta_{\mathbf{k}} = 90°$. Evidently, the streak-like pattern is aligned quite well with these sample ray paths. (We note that reducing discrete particle noise is particularly important to observe the bouncing wave signature.) For reference, the sample rays traveled approximately $0.6R_E$ (or about 6.5°) in the azimuthal direction during half a bounce period, which is a bigger distance than the azimuthal length of the simulation box (1.8° wide).

An interesting feature that stands out in Figure 5b is the sudden drop-off in intensity for $t\Omega_{cp,\mathrm{eq}} \gtrsim 250$ and at $|\lambda_{\mathrm{lat}}| \approx 22.5°$. The border in λ_{lat} is more clearly shown in Figure 5b. This latitude coincides with where ω_{lh}/Ω_{cp} transitions from above 9 to below shown in Figure 3b. Without definitive proof, we surmise that this drop-off in wave energy is related to the sudden disappearance of the 9th harmonic mode above $|\lambda_{\mathrm{lat}}| \approx 22.5°$.

Figure 6 presents the detailed latitudinal variation of wave intensity, which may be compared with experimental data. Figures 6a and 6b show $\langle \delta B^2 + \delta E^2 \rangle_\phi$ and $\langle \delta E^2 \rangle_\phi$, respectively, at $t\Omega_{cp,\mathrm{eq}} = 60$, 150, 240, and 310. Before the primary maximum intensity is reached at $t\Omega_{cp,\mathrm{eq}} \approx 150$, the latitudinal profile exhibits a local minimum in intensity at the equator and two maxima off the equator, indicating that the excitation actually starts first at high latitude. As time goes on, these two maxima move toward the equator to form a single maximum at the equator, as shown in Figures 5a and 5b. Approximately at $t\Omega_{cp,\mathrm{eq}} = 150$, the primary maximum in intensity is reached. As suggested earlier, the wave energy is contained well within $\pm 10°$ latitude, because the difference in intensity is more than an order of magnitude. More quantitatively, the dashed line superimposed in Figure 6a is an exponential fit ($\sim e^{-a|\lambda_{\mathrm{lat}}|}$) to the $t\Omega_{cp,\mathrm{eq}} = 150$ profile (purple curve) with an e-folding value of approximately 0.3. Subsequently, a secondary enhancement off the equator reaches its maximum in intensity around $t\Omega_{cp,\mathrm{eq}} = 240$. Because the waves near the equator have decayed away slightly by this time, the intensity profile exhibits a broader peak extending beyond $|\lambda_{\mathrm{lat}}| = 10°$. Although the intensity as a function of latitude no longer exhibits the exponential behavior, an exponential fit suggests an e-folding value of about 0.16. Finally, the green curve shows the intensity profile at $t\Omega_{cp,\mathrm{eq}} = 310$ at which time many of the off-equatorial waves have converged at the equator. Consequently, the e-folding value increases again to approximately 0.21. As one can see, the contribution of the electric field to the total wave energy is negligible for $\lambda_{\mathrm{lat}} \lesssim 20°$ at all times.

In Figure 6c, the maximum wave intensities at given latitudes are plotted versus latitude. A rectangular box ($5\Omega_{cp,\mathrm{eq}}^{-1}$ long in time and 20 grid points wide in latitude) smoothing is applied to Figures 5a and 5b prior to this analysis. This can be compared with the local simulation results by Min and Liu (2020, Figure 2). The large drop in intensity at high latitude indicates that MSWs are not efficiently tapping into the free energy there. As soon as a wave starts growing, it is refracted equatorward due (mainly) to the gradient of the background magnetic field (see the sample rays in Figure 5d) and thus moves out of the region where the growth rate is positive (e.g., Boardsen et al., 2016). On the other hand, the latitudinal dependence of the relative strength between the electric and magnetic fields is largely consistent with the local simulation results. Figure 6d plots the time when the maximum values (saturation times) were taken. Focusing on $\lambda_{\mathrm{lat}} \lesssim 20°$, the times when the maximum values are reached are consistent with the two-group-wave interpretation mentioned earlier.

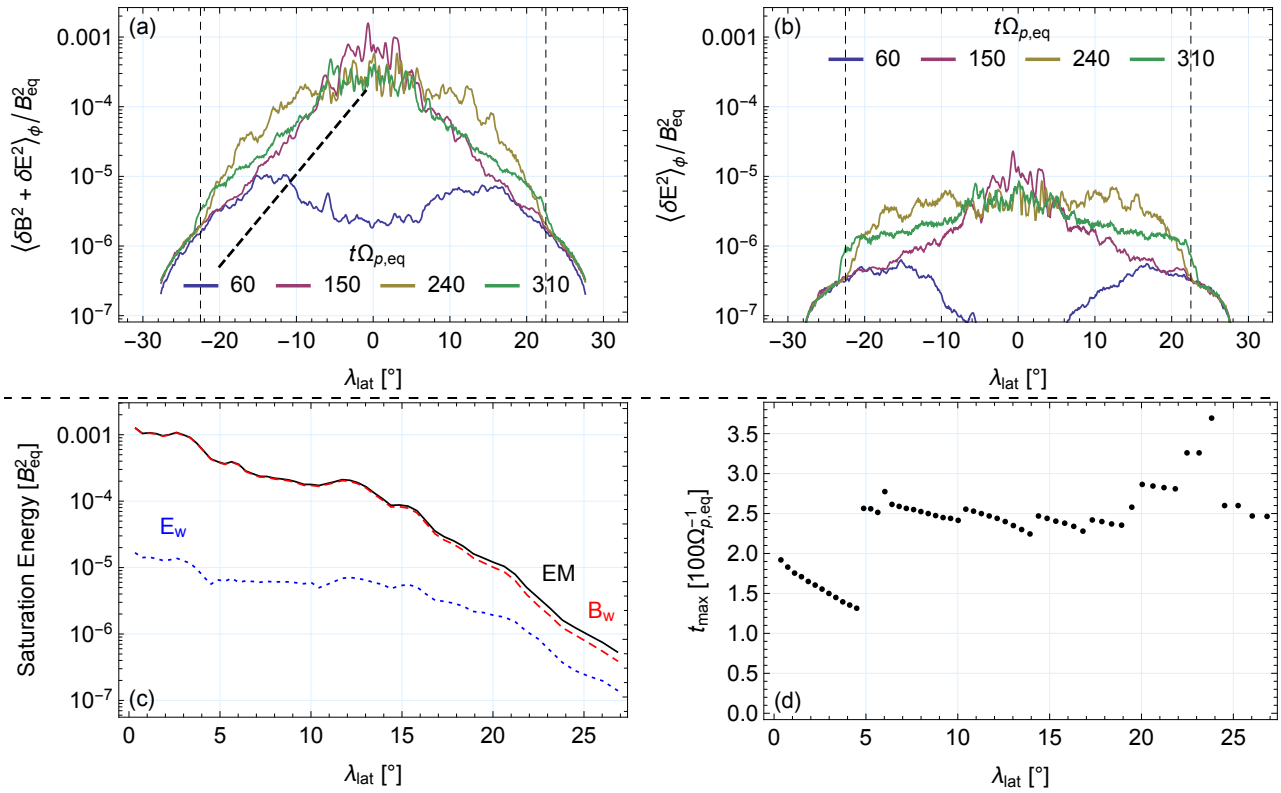

Figure 6. (a) Total wave intensity, $\langle \delta B^2 + \delta E^2 \rangle_\phi$, as a function of latitude at the times labeled (also indicated by horizontal dashed lines of the same colors in Figures 5a and 5b). The dashed line in the southern hemisphere of Figure 6a is an exponential fit to the curve at $t\Omega_{cp,eq} = 150$ with an e-folding value of 0.3. (b) Electric field wave intensity, $\langle \delta E^2 \rangle_\phi$, as a function of latitude at the same times. The vertical dashed lines are drawn at $\pm 22.5°$ latitudes. (c) Maximum wave intensity (or saturation energy) at a given latitude. The labels Bw, Ew, and EM denote the magnetic, electric, and total wave intensity, respectively; and (d) the time of saturation at a given latitude.

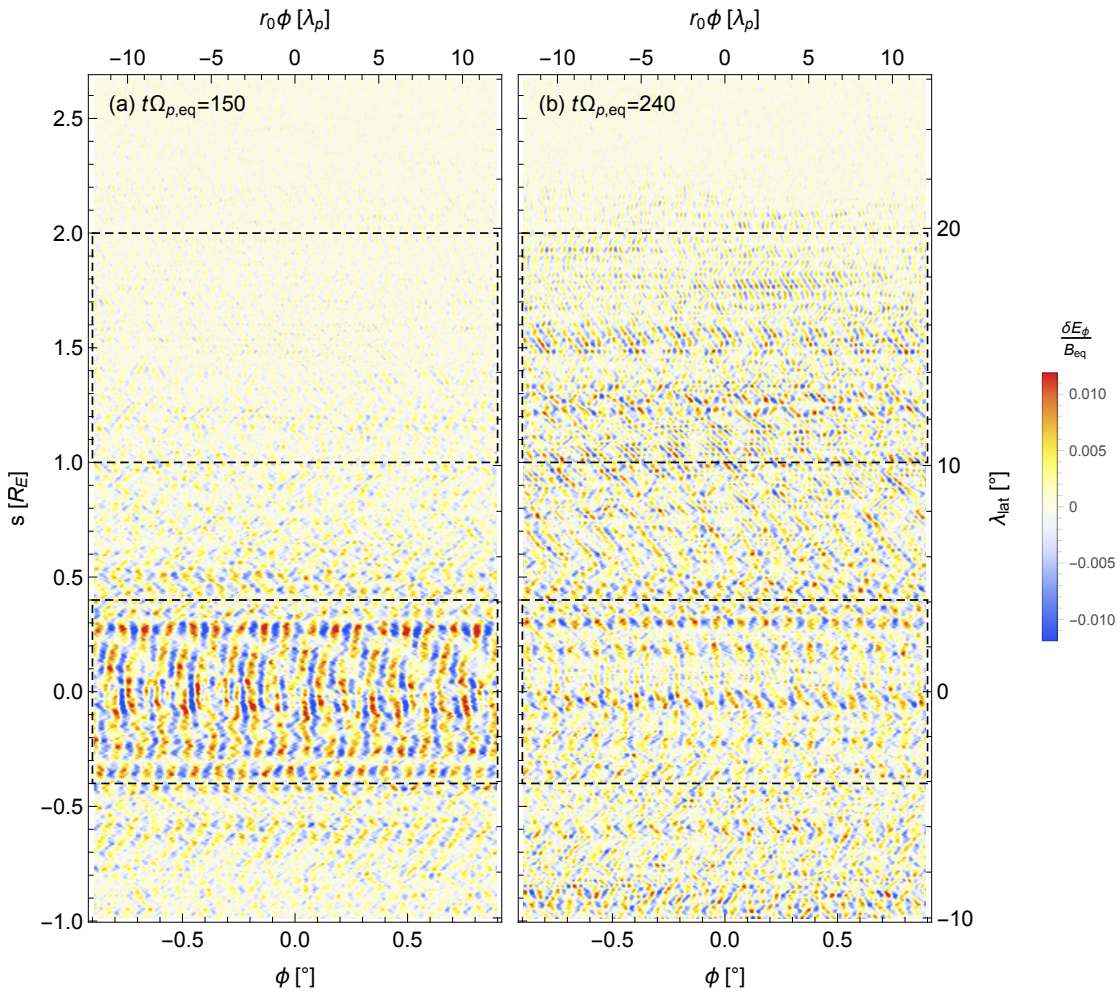

Figure 7. Snapshots of δE_ϕ at $t\Omega_{p,\mathrm{eq}} = 150$ and 240 displayed in (ϕ, s) coordinate space. In addition, the right axis displays magnetic latitude, and the top axis displays $r_0\phi$ in units of the proton inertial length, λ_p.

4.2 Wave Field Structure and Frequency Spectrum

This subsection describes the spatial wave field structure and the power spectral density distribution in frequency and wave number space.

Figure 7 shows two snapshots of δE_ϕ at $t\Omega_{p,\mathrm{eq}} = 150$ and 240 in (ϕ, s) coordinate space. Note that the dipole magnetic field is parallel to the vertical axis and perpendicular to the horizontal axis. The wave fronts are much more complex than those in Chen et al. (2018); part of the reason is that waves propagating left and right are mixed together due to the periodic boundary conditions used in the azimuthal direction, forming the criss-cross pattern of wave fronts. Nevertheless, one may appreciate that the wave fronts are relatively vertical in the vicinity of the equator (between the two horizontal dashed lines drawn at $\lambda_{\mathrm{lat}} = \pm 4°$), especially during the primary wave intensity maximum (Figure 7a), and become quickly oblique outside. Movies included in supporting information show that propagation of MSWs is dominantly in the azimuthal direction (i.e., quasi-perpendicular to the dipole magnetic field). Also, consistent with the Poynting flux shown in Figure 5c, MSWs off the equator converge toward the equator, and eventually propagate to the opposite hemispheres near the end of the simulation.

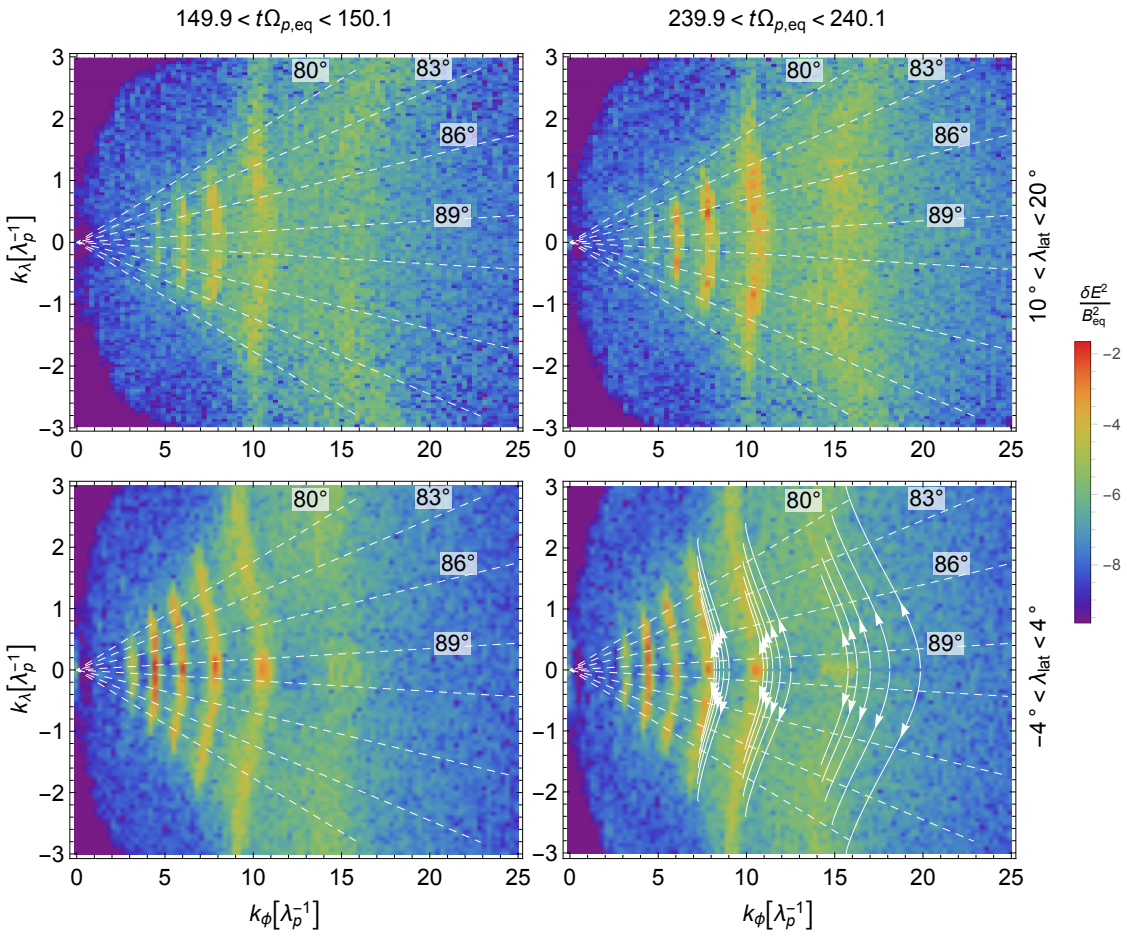

Figure 8. Electric field power spectral density in wave number space. The corresponding latitudinal extent and time are displayed at the top and right axes of the panels. The parallel (k_λ) and perpendicular (k_ϕ) wave numbers are normalized to the proton inertial length, λ_p. The harmonic numbers can be identified as follows: the outermost discrete mode at $k_\phi \lambda_p \approx 15$ is the 8th harmonic mode, and one can count from there one by one toward smaller k_ϕ. The dashed lines radiating from the origin correspond to $\theta_{\mathbf{k}} = 80$, 83, 86, and 89° as labeled. The white curves in the lower-right panel are paths of sample rays in wave number space corresponding to the 6th, 7th, and 8th harmonics. For each harmonic, five rays were traced starting from 15, 17, 19, 21, and 23° latitudes (from the leftmost to rightmost curves) with an initial wave normal angle $\theta_{\mathbf{k}} = 90°$. Tracing ended when the rays arrived at the equator.

To get a more quantitative understanding of the wave power distribution in $\theta_{\mathbf{k}}$ space, we took a Fourier transform of the simulated wave fields in two latitudinal ranges of $-4^\circ < \lambda_{\rm lat} < 4^\circ$ and $10^\circ < \lambda_{\rm lat} < 20^\circ$, as marked by the horizontal dashed lines in Figure 7. The result is shown in Figure 8. For reference, Min and Liu (2020, Figure 4) shows the linear instability growth rates and the wave spectral densities from local two-dimensional PIC simulations. Wave power spans up to the $\theta_{\mathbf{k}} = 80^\circ$ marks at around 15° latitudes, and beyond $\theta_{\mathbf{k}} = 77^\circ$ around the equator. The major difference between the equatorial and off-equatorial waves is the pronounced presence of quasi-perpendicular propagating modes (within the $\theta_{\mathbf{k}} = 89^\circ$ marks). At the equator, there are isolated peaks in wave power at $\theta_{\mathbf{k}} \approx 90^\circ$ essentially for all harmonics, whereas there is a local minimum of wave power at $\theta_{\mathbf{k}} = 90^\circ$ in the latitudinal range of $10^\circ < \lambda_{\rm lat} < 20^\circ$. (In comparison, the local simulations of Min and Liu (2020) produced dominant wave power at $\theta_{\mathbf{k}} = 90^\circ$ in this latitudinal range). The power-weighted average wave normal angle at $t\Omega_{cp,\rm eq} = 150$ is about $\theta_{\mathbf{k}} = 87^\circ$ at the equatorial region and $\theta_{\mathbf{k}} = 85^\circ$ in the latitudinal range of $10^\circ < \lambda_{\rm lat} < 20^\circ$. Due to the wide spread of power in $\theta_{\mathbf{k}}$ space at the equator, the difference is actually only a few degrees at most. At the later time, the average $\theta_{\mathbf{k}}$ values are 85° at the equator and 86° in the latitudinal range of $10^\circ < \lambda_{\rm lat} < 20^\circ$. Also, it should be noted that the power-weighted average wave normal angle near the equatorial region will vary depending on the size of the latitudinal range we choose.

To better understand the spectral pattern, the trajectories of sample rays are superimposed in the lower-right panel of Figure 8. Three groups of rays corresponding to the 6th, 7th, and 8th harmonics, respectively, were traced. In each group, five rays were launched from 15, 17, 19, 21, and 23° latitudes (from the leftmost to rightmost curves in each ray bundle) with an initial wave normal angle $\theta_{\mathbf{k}} = 90^\circ$. Tracing ended when the rays arrived at the equator. The locations where the rays landed in wave number space line up quite well with the strips of enhanced power, indicating their off-equatorial origin. (In comparison, the local simulation result gives a very different spectral pattern; see Min and Liu (2020, Figure 4).) In contrast, the waves at $\theta_{\mathbf{k}} = 90^\circ$ do not connect to any off-equatorial rays, hence consistent with the interpretation that they were generated locally.

Figure 9 shows short-time frequency spectrograms at 0, 5, 10, and 15° latitudes, which are more relevant to experimental data analyses. The window size is around $42\Omega_{cp,\rm eq}^{-1}$ long. At the equator, there are multiple discrete spectral peaks, on top of a weaker, more continuous spectrum extending beyond ω_{lh}. The discrete spectral peaks are found at harmonics of Ω_{cp} (from 3rd to 7th by visual inspection; see the vertical scale on the right side of the panel), indicating that they have been excited locally. On the other hand, the waves corresponding to the continuous spectrum should have their source off the equator. The relative strength of the discrete modes (i.e., of the local origin) compared to the continuous mode (i.e., of the off-equator origin) decreases with increasing latitude, and at 15° latitude only the 5th harmonic (which is the fastest growing mode at that latitude (see Min & Liu, 2020, Figure 4)) is barely seen (see the vertical scale on the right side of the panels). Hence, the continuous spectrum dominates there.

Some studies analyzed the frequency-latitude dependent wave power distributions. We can of course deploy virtual satellites along a field line in the simulation to capture time-series of electric and magnetic fields. Figure 10 shows the electric and magnetic field spectrograms within two temporal spans, $118.6 < t\Omega_{cp,\rm eq} < 181.4$ and $208.6 < t\Omega_{cp,\rm eq} < 271.4$. For guidance, the white dashed curves denote integer multiples of Ω_{cp}, and the black dotted curves indicate ω_{lh}/Ω_{cp}. One can immediately see that the latitude at which a given harmonic mode disappears below the noise level is an increasing function of the harmonic number. This is approximately consistent with the latitude at which the growth rates of the corresponding harmonics become negative as indicated by the open circles in the top-left panel. Note that such a behavior is related to the varying v_s/v_A ratio at different latitude as well as equatorward propagation of MSWs excited near the harmon-

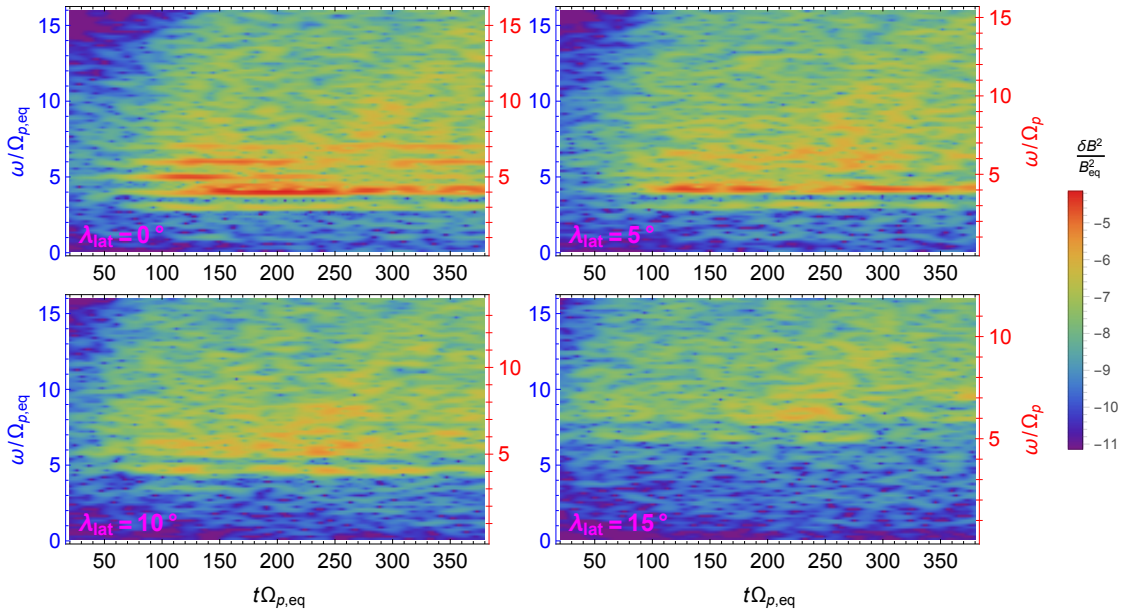

Figure 9. Short-time frequency spectrograms of the fluctuating magnetic field at 0, 5, 10, and 15° latitudes. In each panel, the left blue tick marks denote frequency normalized by $\Omega_{cp,\mathrm{eq}}$, and the right red tick marks denote frequency normalized by Ω_{cp}, the local proton cyclotron frequency.

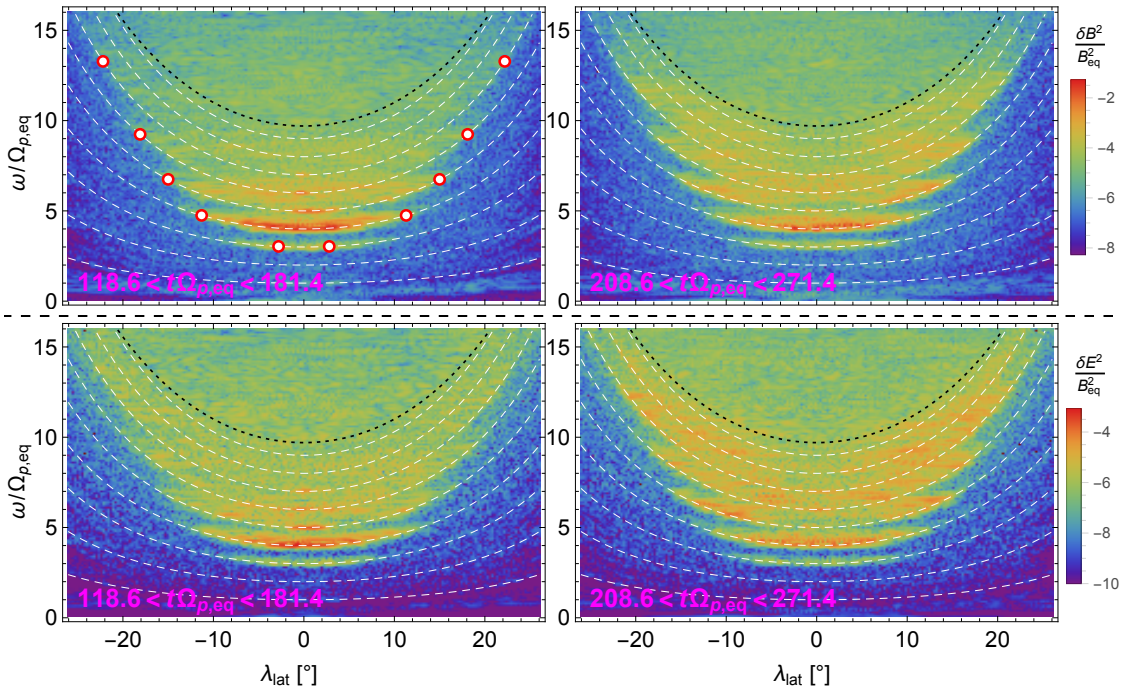

Figure 10. Frequency-latitude power spectral densities of the fluctuating magnetic field (top) and electric field (bottom). The left and right columns correspond to two different time spans, $118.6 < t\Omega_{cp,\mathrm{eq}} < 181.4$ and $208.6 < t\Omega_{cp,\mathrm{eq}} < 271.4$, respectively. For guidance, the white dashed curves denote integer multiples of Ω_{cp}, and the black dotted curves indicate ω_{lh}/Ω_{cp}. The red open circles in the top-left panel mark the latitudes at which the growth rates of the various harmonic modes shown in Figure 3c turn negative.

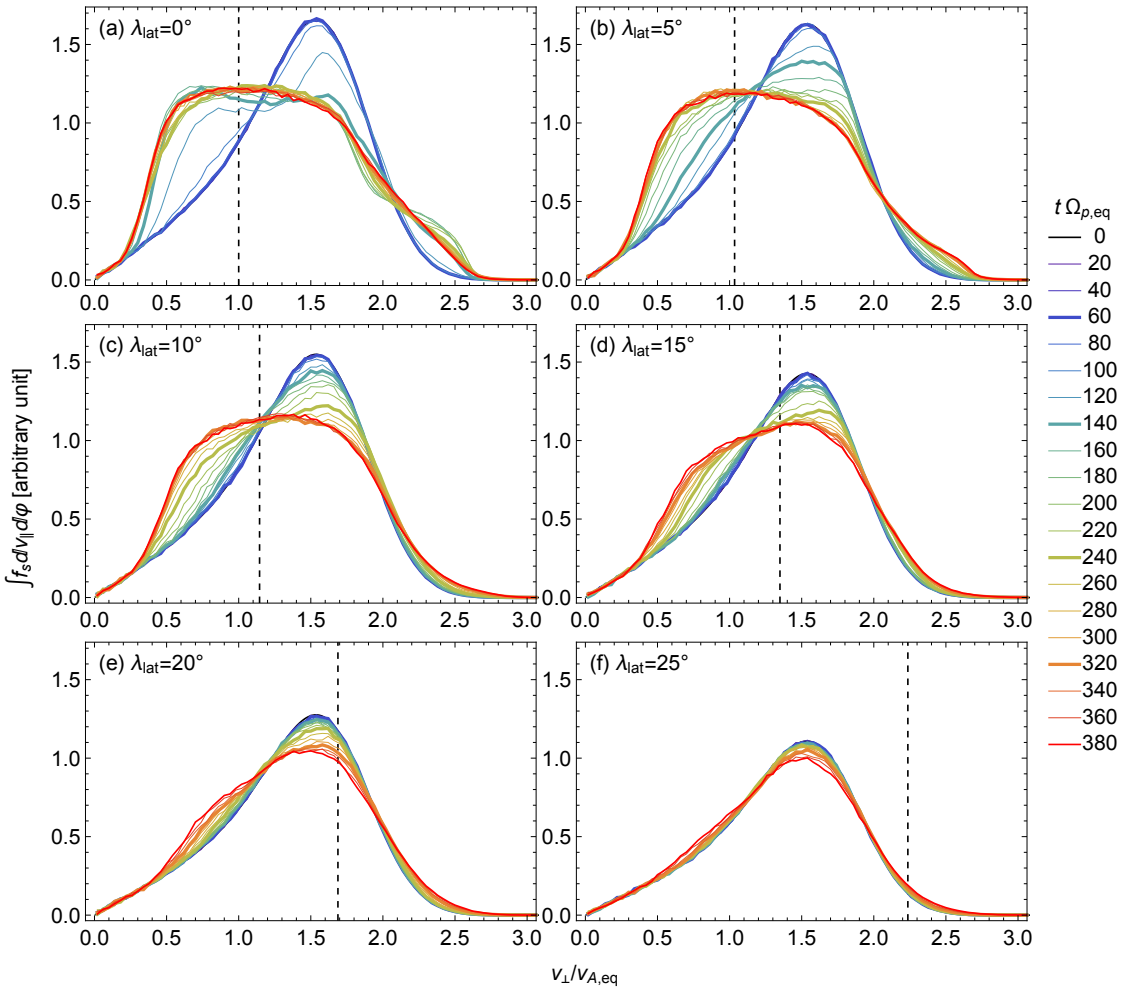

Figure 11. Temporal evolution of the energetic partial shell proton distributions sampled at latitudes $\lambda_{\rm lat} = 0$, 5, 10, 15, 20, and 25°. Line color denotes times as labeled, with the thicker lines approximately corresponding to the time slices in Figures 6a and 6b. The vertical dashed lines mark the local Alfvén speed, v_A.

ics of Ω_{cp} (manifested as diffuse wave power in frequency space). Although the reduced m_p/m_e and $c/v_{A,\rm eq}$ used in our simulation limit MSWs to a narrower frequency range than observed, the outline of the spectral power in latitude-frequency space resembles the funnel-shaped spectrograms discussed by Boardsen et al. (1992, 2016). In addition, it is only the low frequency part of the spectrum near the equator that exhibits discrete spectral peaks.

4.3 Evolution of Partial Shell Proton Distribution

In this section, we examine the temporal evolution of energetic partial shell protons along the field line. Figure 11 shows the reduced velocity distribution functions, $\int_{-\infty}^{\infty}\int_{0}^{2\pi} f_s d\phi dv_{\parallel}$, as a function of the perpendicular velocity, $v_{\perp}$, sampled at several different latitudes. (For reference, the reduced distribution functions from local two-dimensional simulations (Min & Liu, 2020) are included in the supporting information, Figure S5.) The excited MSWs scatter the protons to reduce the positive slope (and also the negative slope beyond the peak of the initial distribution) of the energetic partial shell proton distribution func-

tions in a wide latitudinal range. The degree to which the scattering occurs is strongly dependent upon latitude. The distribution function at 25° latitude has barely changed (cf. Figure S5), whereas energetic protons near the equator experienced the largest scattering. Interestingly (but not surprisingly), this trend has a correlation with the local wave intensity shown in Figures 5a and 5b. The evolution of the distribution function at the equator is pretty much finished between $60 < t\Omega_{cp,\mathrm{eq}} < 140$, during which exponential growth and saturation of near-equatorial MSWs occurred. Meanwhile, the distribution functions at 10 and 15° latitudes exhibit the largest change between $140 < t\Omega_{cp,\mathrm{eq}} < 240$, which corresponds to the growth and saturation of off-equatorial MSWs (aided by seed fluctuations from opposite hemispheres). Finally, at 20° latitude, this time is further delayed so that the largest change in the distribution function occurs between $240 < t\Omega_{cp,\mathrm{eq}} < 320$. On the other hand, since the wave intensity profile exhibits a sudden drop at around 23° latitude, the MSWs beyond this boundary are simply not strong enough to cause substantial scattering at 25° latitude. (The slight scattering there might have been caused by the numerical noise instead.)

In comparison with the local two-dimensional simulations of Min and Liu (2020) (see also Figure S5), there is still plenty of free energy left at high latitudes, and in fact, Figure 5b indicates trickling MSW excitation at later times. This is evidence that the off-equatorial MSWs do not harness that free energy available efficiently because of the strong equatorward refraction there and rapid detuning of resonance as waves propagate, unless the background seed fluctuations are sufficiently strong. (The low-resolution test simulations indeed showed much faster evolution of the high-latitude distribution functions (Boardsen et al., 2019).)

A comparison of Figures 11a and 11f clearly suggests that the energetic proton distribution at $\lambda_{\mathrm{lat}} = 25°$, which experienced little scattering, cannot simply be constructed by projecting the equatorial distribution according to Liouville's theorem, which experienced the most scattering. This indicates that the scattering of the energetic protons and the evolution of their distribution functions are most likely local, despite an expectation that mixing due to the field-aligned motion of particles would wash away any local effect. The bounce period in a dipole field is given by $\tau_b \approx (r_0/\sqrt{W_p/m_p})(3.7 - 1.6\sin\alpha_{\mathrm{eq}})$, where W_p is the kinetic energy of the particle (Roederer, 1970). Plugging in the representative parameters for the partial shell protons, $r_0 = 770\lambda_{p,\mathrm{eq}}$, $W_p = m_p v_s^2/2$, and $\alpha_{\mathrm{eq}} = 60°$, yields $\tau_b \approx 1,480\Omega_{cp,\mathrm{eq}}^{-1}$. Since the total simulation duration (which is about $380\Omega_{cp,\mathrm{eq}}^{-1}$) is roughly a quarter bounce period, the time scale of MSW excitation (roughly $80\Omega_{cp,\mathrm{eq}}^{-1}$) is, in fact, shorter than the bounce period of the partial shell protons.

Figure 12 shows a comparison between the locally sampled partial shell proton distributions (black curve) and the distributions mapped from the instantaneous equatorial distributions following Liouville's theorem (red curve). The Liouville equilibria are maintained initially up to $t\Omega_{cp,\mathrm{eq}} = 80$ for all latitudes, during which MSW activity is low. Then, during the near-equatorial MSW saturation at $t\Omega_{cp,\mathrm{eq}} = 150$ the two types of distributions exhibit the largest deviation, even at as low a latitude as $\lambda_{\mathrm{lat}} = 5°$, because the equatorial partial shell distribution is modified greatly as a result of the rapid MSW excitation but the partial shell protons had no time to communicate the local effect to other latitudes. After that, the equilibrium is quickly restored at $\lambda_{\mathrm{lat}} = 5°$, and mostly at $\lambda_{\mathrm{lat}} = 10°$ by the end of the simulation. However, the distribution at $\lambda_{\mathrm{lat}} = 20°$ still exhibits a large deviation (mostly at the low energy regime) at the end of the simulation. Notably, the rate at which the equilibrium is restored is energy-dependent, in accordance with the bounce period being energy-dependent.

5 Discussion

We stopped the simulation at $t\Omega_{cp,\mathrm{eq}} = 380$ for a few reasons. Practically, we already spent many cpu hours (more than a month worth of time); and from the physics

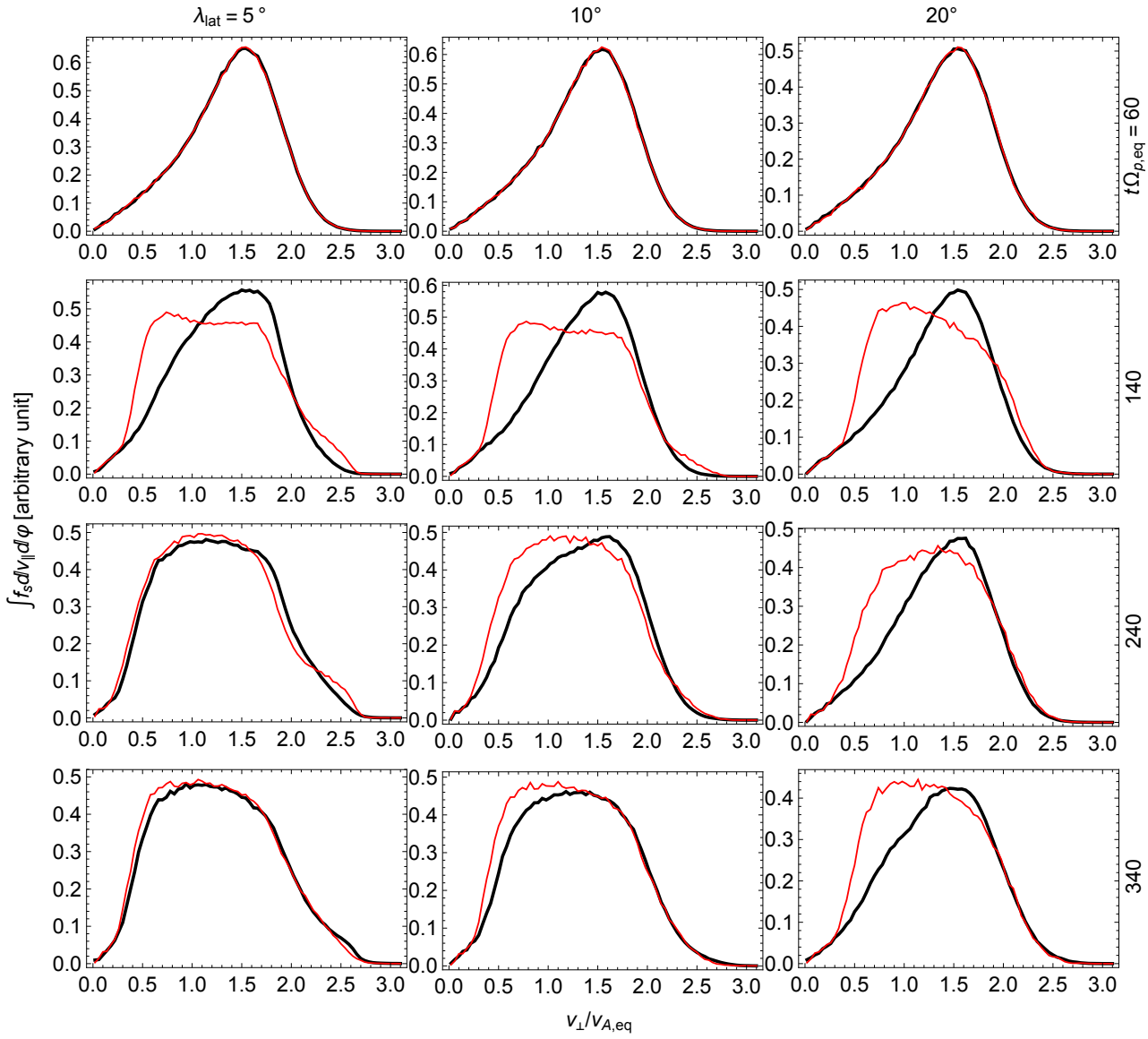

Figure 12. A comparison between the locally sampled partial shell proton distributions (black curve) and the distributions mapped from the instantaneous equatorial distributions following Liouville's theorem (red curve). The columns correspond to the selected latitudes (5, 10, and 20°; top labels) and the rows correspond to the times of the distribution snapshots (60, 140, 240, and $340\Omega_{cp,\mathrm{eq}}^{-1}$; right labels).

point of view, the system already passed the quasilinear saturation phase and was nearing an equilibrium state. In addition, since our two-dimensional simulation domain does not allow radial propagation of MSWs which tend to refract radially outward in the dipole field (unless there exists a steep density gradient), we were not tempted to continue the simulation and draw conclusions about the long-term behavior that might not be justified. On the other hand, under a suitable circumstance, namely at the plasmapause (Kasahara et al., 1994; Chen & Thorne, 2012), MSWs can indeed propagate in the azimuthal direction even beyond the source region with little radial refraction. Motivated by this and also to understand the propagation outside the source region, we removed all the energetic partial shell protons in the system and continued the simulation afterwards. Since these results are not essential for the conclusions of the present study, we include the summary figures (similar to Figure 5) of this "long-term" simulation in the supporting information and only state a few notable results here (see Figures S6 and S7). Since there is no damping/growth, the MSWs thereafter continue propagating azimuthally while bouncing up and down latitudinally. The magnetic field energy is contained well within $\lambda_{\rm lat} = \pm 10^\circ$, whereas the electric field energy has a non-negligible presence up to $\lambda_{\rm lat} = \pm 15^\circ$, still consistent with the conclusion derived earlier. Since the time scale for the continuous MSW excitation is shorter than the wave packet bounce period (see Figures 5a and 5b), the wave packets are not uniform in time and latitude, resulting in the bunching of wave packets and the modulation of amplitudes in time and latitude. Contrary to the dominant equatorward Poynting flux during the MSW growth phase, the Poynting flux outside the source region clearly exhibits a bi-directional nature along the field line. Overall, it appears that we would have gotten the same propagation pattern, had we traced a bundle of rays with the amplitudes prescribed from the last point of the present simulation.

Since the present simulation is for one parameter set, it would be premature to generalize the present results for all possible combinations of key parameters. Nevertheless, we make a few remarks on observation-simulation comparison. Recent statistical studies, particularly Boardsen et al. (2016) and Zou et al. (2019), have carried out comprehensive analyses of wave properties involving latitudinal dependence. It has been consistently shown that MSWs are most frequently observed near the magnetic equator, which any rightful model must demonstrate. Our simulation also showed a peak in intensity centered at the magnetic equator, and this was achieved without localizing the free energy source to the magnetic equator. At the time of the primary wave saturation, the difference in wave intensity at the equator and at $\lambda_{\rm lat} = 10^\circ$ was more than one order of magnitude. At later times, however, the difference in magnitude was reduced, which led to a broader peak of wave intensity versus latitude. Both Boardsen et al. (2016) and Zou et al. (2019) have shown a similar trend, but the slope of wave intensity with respect to latitude does not seem to agree: Zou et al. (2019, Figure 3) shows a much narrower intensity peak with a steeper slope compared with Boardsen et al. (2016, Figures 10 and 11). Our result appears, at least for the present parameters, to be more consistent with the result of Boardsen et al. (2016). We note that the present value for the equatorial temperature anisotropy of energetic protons is small ($A = 0.5$). The statistical study by Thomsen et al. (2017) showed a wide range of A values, reaching as large a value as 10. So, since the source region can be further confined to the equatorial region for a larger anisotropy of energetic protons (but not too large to excite EMIC waves), the use of a value for A larger than assumed here can be one way to achieve the steeper gradient of the MSW amplitudes shown by Zou et al. (2019).

On the other hand, the fact that the energetic partial shell protons do not necessarily follow Liouville's theorem during MSW excitation begs a question of whether initializing the energetic protons according to Liouville's theorem in the simulation was really necessary. It could be that in reality the energetic ring-like protons (and hence the source region) are indeed localized close to the magnetic equator by some physical mechanisms (such as injections), in which case Chen et al. (2018) may have been on the right

track. This suggests another way to achieve a steeper gradient of the MSW amplitudes, where one takes a similar approach to Chen et al. (2018) but limiting the free energy source near the magnetic equator without making the equatorial distribution unrealistically anisotropic. Observationally, there may be two ways to judge which mechanism is more likely. First is to explicitly measure whether there exists an extended ring-like feature during MSW excitation using multi-spacecraft situated along the same field line; and second is to check the direction of Poynting flux: A signature of converging Poynting flux may be indicative of the extended source scenario.

Another recent notable result is the latitudinal dependence of the average wave normal angle produced by Zou et al. (2019). They reported that the median of wave normal angles maximizes at the equator and monotonically decreases with latitude (see Zou et al., 2019, Figures 5 and 6). The median wave normal angle starts out from around 88° at the equator, falls monotonically with latitude, and reaches around 85.5° at 15° latitude. If this trend is a reasonable representation for the dominant wave modes, our simulation seems to demonstrate a trend similar to their statistical study. Before hastily jumping to the conclusion, however, we should note that Zou et al. (2019) made, as far as their paper is concerned, no attempt to understand the impact of the larger error in $\theta_{\mathbf{k}}$ associated with individual $\theta_{\mathbf{k}}$ measurements and how it would impact their fitted curves. Boardsen et al. (2016) estimated for the $\theta_{\mathbf{k}}$ measurements greater than 89.5° the error in $\theta_{\mathbf{k}}$ to be 2.54° on average, based on eigenvalue analysis. Also, they showed using simulated data composed of multiple sine waves with randomly assigned $\theta_{\mathbf{k}}$ between 87 and 90° that for the 55.6 Hz EMFISIS survey channel (Kletzing et al., 2013) the error in $\theta_{\mathbf{k}}$ was 5.6° and that the spread in $\theta_{\mathbf{k}}$ derived from polarization analysis of the simulated data was similar to that of the observations (Boardsen et al., 2016, Figures 4 and 5). Therefore, one does see a trend in $\theta_{\mathbf{k}}$ with latitude in the EMFISIS survey data, but it seems unclear as to what this trend means. Whether the observations corroborate our simulation results or not, understanding how the MSW field structure varies with latitude is important to quantitatively diagnose the resonant and non-resonant effect of MSWs on energetic radiation belt electrons. So, a future study based on rigorous statistical analysis with more accurate $\theta_{\mathbf{k}}$ measurements must be done to sort this out.

6 Conclusions

Here, two-dimensional PIC simulations were carried out with a simulation box on a constant L-shell surface. Compared with the recent two-dimensional PIC simulation study of MSWs in a meridional plane (Chen et al., 2018), the use of such an unconventional simulation domain was motivated by the recent observational studies wherein propagation of MSWs in the source region is dominantly in the azimuthal direction. Furthermore, we used a partial shell velocity distribution at the equator for energetic protons which is only mildly anisotropic and therefore more realistic. This resulted in a wide latitudinal extent of the free energy source following Liouville's theorem. Overall, the present simulation differed most significantly in these two aspects from the recent simulation study in dipole geometry of Chen et al. (2018), and therefore, the results presented here can be a good complement, or contrast, to theirs.

On the other hand, as in most PIC simulations, we had to use a reduced proton-to-electron mass ratio and a smaller than realistic value for the light-to-Alfvén speed ratio in order to reduce computation time. This altered the number of MSW harmonics in the system and the time scale of MSW evolution. Nevertheless, the wave dispersion relation was not greatly affected by the reduced ratios used and MSWs were driven by the same physics. So, we can still get insight into the MSW generation process in the presence of inhomogeneity along the field line, which is the primary goal of the present study. Also, the dominant background proton and electron populations were assumed to be cold. This helped lower the background noise floor in the simulation. Finally, in a three-dimensional simulation domain the radial gradient of the dipole magnetic field

and the plasma density would cause MSWs to typically refract radially outward, while the present two-dimensional setup forced wave packets to remain in one L-shell. This will not be a problem in the early stage of the simulation, but one may need to exercise caution when interpreting the present results at later times.

The wave propagation and spectral characteristics presented here can be largely understood from the purview of linear instability theory for local homogeneous plasmas and the geometric optic framework for wave propagation in an inhomogeneous medium. In fact, ray tracing is based upon these two principles. The main strength of the present approach is that the wave and particle dynamics are self-consistently handled. Here are some notable results.

1. Despite the extended unstable region in latitude owing to the use of a mild equatorial temperature anisotropy of the ring-like protons, MSWs excited at high latitude are refracted equatorward and do not fully harness free energy available for their amplification. This is consistent with the previous explanation (Boardsen et al., 1992, 2016) that the equatorward refraction due to the field line gradient of the dipole magnetic field prevents the high-latitude MSWs from staying in resonance (such that particle free energy is transferred to waves) with the energetic protons for a sufficiently long time. On the other hand, the MSWs excited at the equator experience much larger amplification, owing to the vanishing magnetic field gradient there.
2. While exhausting free energy only slowly, the off-equatorial MSWs exhibit the signatures of refraction and reflection suggested by the ray tracing analyses. In addition, the off-equatorial MSWs experience amplification at or near the reflection points (where $\theta_{\mathbf{k}}$ goes through 90°) and are probably damped when crossing the equator (where the wave normal direction is farthest from the perpendicular direction). The Poynting flux is dominantly convergent toward the equator during MSW growth and saturation, with occasional signatures of penetration across the equator to the opposite hemispheres.
3. The MSWs in the present simulation exhibit a rather complex wave field structure varying with latitude. The simulated wave fronts are roughly aligned with the dipole field in the vicinity of the equator (within $\sim \pm 4°$ latitude), and are slanted somewhat away from that direction at higher latitude. Around 15° latitude the power-weighted average wave normal angle is about 85°, and near the equatorial region it is about 87° during the primary maximum of wave intensity; the latter number varies depending on the relative strength between the waves originating at the equator or off-equator.
4. In the equatorial region, the locally generated MSWs and the transient MSWs of off-equatorial origin coexist. As a result, close to the equatorial region, the simulated frequency spectrograms exhibit both discrete spectral peaks at harmonics of the local proton cyclotron frequency (to which the MSWs of the equatorial origin contribute) and a broad continuous spectrum extending beyond the lower hybrid frequency (to which the MSWs of the off-equatorial origin contribute). With an increasing latitude, the discrete peaks weaken gradually and the continuous spectrum eventually dominates (at about 15°), as a result of rapid detuning of resonance as waves propagate and get refracted. In addition, the lower cutoff of the unstable harmonics also shifts toward high harmonic number with an increasing latitude so that the frequency-latitude spectrogram demonstrates the so-called funnel-shaped structure.
5. Consistent with the quasilinear picture, energetic protons sampled at several latitudes experience scattering in response to the MSW excitation in such a way as to reduce the positive slope of the proton velocity distribution function in the perpendicular velocity direction. The degree to which the scattering occurs has a good correlation with the instantaneous MSW intensity at a given latitude. Further-

more, the local energetic proton distributions do not follow Liouville's theorem on the time scale of MSW excitation.

Acknowledgments

This work was supported by the National Research Foundation of Korea (NRF) grant funded by the Korea government (MSIT) (No. 2020R1C1C1009996) and by research fund of Chungnam National University. K.L.'s research is supported by National Natural Science Foundation of China (NSFC) grant 41974168. Work at Dartmouth was supported by NSF grant AGS-1602469 and also by NASA grant 80NSSC19K0270. F. Němec would like to acknowledge the use of funds from GACR grant 18-00844S. At Goddard this study was supported by NASA prime contract NAS5-01072. Resources and technical support for simulations were provided by Korea Institute of Science and Technology Information (KSC-2019-CRE-0003). The numerical simulations were also performed by using a high performance computing cluster at the Korea Astronomy and Space Science Institute. Reduced datasets to produce the figures as well as the code used here are available in a Zenodo data repository at (doi: 10.5281/zenodo.3894005).

References

André, R., Lefeuvre, F., Simonet, F., & Inan, U. S. (2002, Jul). A first approach to model the low-frequency wave activity in the plasmasphere. *Annales Geophysicae*, *20*(7), 981-996. doi: 10.5194/angeo-20-981-2002

Boardsen, S. A., Gallagher, D. L., Gurnett, D. A., Peterson, W. K., & Green, J. L. (1992, October). Funnel-shaped, low-frequency equatorial waves. *J. Geophys. Res.*, *97*, 14. doi: 10.1029/92JA00827

Boardsen, S. A., Hospodarsky, G. B., Kletzing, C. A., Engebretson, M. J., Pfaff, R. F., Wygant, J. R., ... De Pascuale, S. (2016, April). Survey of the frequency dependent latitudinal distribution of the fast magnetosonic wave mode from Van Allen Probes Electric and Magnetic Field Instrument and Integrated Science waveform receiver plasma wave analysis. *Journal of Geophysical Research (Space Physics)*, *121*, 2902-2921. doi: 10.1002/2015JA021844

Boardsen, S. A., Hospodarsky, G. B., Min, K., Averkamp, T. F., Bounds, S. R., Kletzing, C. A., & Pfaff, R. F. (2018, August). Determining the Wave Vector Direction of Equatorial Fast Magnetosonic Waves. *Geophys. Res. Lett.*, *45*, 7951-7959. doi: 10.1029/2018GL078695

Boardsen, S. A., Min, K., Liu, K., Denton, R. E., & Nemec, F. (2019, December). Particle-in-cell simulations of fast magnetosonic waves on a drift shell surface in the dipole magnetic field. In *Agu fall meeting abstracts* (Vol. 2019, p. SM51F-3251).

Bortnik, J., & Thorne, R. M. (2010, July). Transit time scattering of energetic electrons due to equatorially confined magnetosonic waves. *Journal of Geophysical Research (Space Physics)*, *115*, A07213. doi: 10.1029/2010JA015283

Chen, L. (2015, June). Wave normal angle and frequency characteristics of magnetosonic wave linear instability. *Geophys. Res. Lett.*, *42*, 4709-4715. doi: 10.1002/2015GL064237

Chen, L., Maldonado, A., Bortnik, J., Thorne, R. M., Li, J., Dai, L., & Zhan, X. (2015, August). Nonlinear bounce resonances between magnetosonic waves and equatorially mirroring electrons. *Journal of Geophysical Research (Space Physics)*, *120*, 6514-6527. doi: 10.1002/2015JA021174

Chen, L., Sun, J., Lu, Q., Wang, X., Gao, X., Wang, D., & Wang, S. (2018, September). Two-Dimensional Particle-in-Cell Simulation of Magnetosonic Wave Excitation in a Dipole Magnetic Field. *Geophys. Res. Lett.*, *45*, 8712-8720. doi: 10.1029/2018GL079067

Chen, L., & Thorne, R. M. (2012, July). Perpendicular propagation of magnetosonic

waves. *Geophys. Res. Lett.*, *39*, L14102. doi: 10.1029/2012GL052485

Chen, L., Thorne, R. M., Jordanova, V. K., & Horne, R. B. (2010, November). Global simulation of magnetosonic wave instability in the storm time magnetosphere. *Journal of Geophysical Research (Space Physics)*, *115*, A11222. doi: 10.1029/2010JA015707

Denton, R. E. (2018, February). Electromagnetic Ion Cyclotron Wavefields in a Realistic Dipole Field. *Journal of Geophysical Research (Space Physics)*, *123*(2), 1208-1223. doi: 10.1002/2017JA024886

Denton, R. E., Jordanova, V. K., & Fraser, B. J. (2014, Oct). Effect of spatial density variation and O+ concentration on the growth and evolution of electromagnetic ion cyclotron waves. *Journal of Geophysical Research (Space Physics)*, *119*(10), 8372-8395. doi: 10.1002/2014JA020384

Gulelmi, A. V., Klaine, B. I., & Potapov, A. S. (1975, February). Excitation of magnetosonic waves with discrete spectrum in the equatorial vicinity of the plasmapause. , *23*, 279-286. doi: 10.1016/0032-0633(75)90133-6

Gurnett, D. A. (1976, Jun). Plasma wave interactions with energetic ions near the magnetic equator. *J. Geophys. Res.*, *81*(16), 2765. doi: 10.1029/JA081i016p02765

Horne, R. B., Thorne, R. M., Glauert, S. A., Meredith, N. P., Pokhotelov, D., & Santolík, O. (2007, September). Electron acceleration in the Van Allen radiation belts by fast magnetosonic waves. *Geophys. Res. Lett.*, *34*, L17107. doi: 10.1029/2007GL030267

Horne, R. B., Wheeler, G. V., & Alleyne, H. S. C. K. (2000, December). Proton and electron heating by radially propagating fast magnetosonic waves. *J. Geophys. Res.*, *105*, 27597-27610. doi: 10.1029/2000JA000018

Hrbáčková, Z., Santolík, O., Němec, F., Macúšová, E., & Cornilleau-Wehrlin, N. (2015, February). Systematic analysis of occurrence of equatorial noise emissions using 10 years of data from the Cluster mission. *Journal of Geophysical Research (Space Physics)*, *120*, 1007-1021. doi: 10.1002/2014JA020268

Hu, Y., & Denton, R. E. (2009, December). Two-dimensional hybrid code simulation of electromagnetic ion cyclotron waves in a dipole magnetic field. *Journal of Geophysical Research (Space Physics)*, *114*, A12217. doi: 10.1029/2009JA014570

Kasahara, Y., Kenmochi, H., & Kimura, I. (1994, July). Propagation characteristics of the ELF emissions observed by the satellite Akebono in the magnetic equatorial region. *Radio Science*, *29*, 751-767. doi: 10.1029/94RS00445

Kletzing, C. A., Kurth, W. S., Acuna, M., MacDowall, R. J., Torbert, R. B., Averkamp, T., ... Tyler, J. (2013, November). The Electric and Magnetic Field Instrument Suite and Integrated Science (EMFISIS) on RBSP. *Space Sci. Rev.*, *179*(1-4), 127-181. doi: 10.1007/s11214-013-9993-6

Laakso, H., Junginger, H., Schmidt, R., Roux, A., & de Villedary, C. (1990, July). Magnetosonic waves above fc(H+) at geostationary orbit - GEOS 2 results. *J. Geophys. Res.*, *95*, 10609-10621. doi: 10.1029/JA095iA07p10609

Li, X., & Tao, X. (2018, January). Validation and Analysis of Bounce Resonance Diffusion Coefficients. *Journal of Geophysical Research (Space Physics)*, *123*, 104-113. doi: 10.1002/2017JA024506

Li, X., Tao, X., Lu, Q., & Dai, L. (2015, November). Bounce resonance diffusion coefficients for spatially confined waves. *Geophys. Res. Lett.*, *42*, 9591-9599. doi: 10.1002/2015GL066324

Liu, K., Gary, S. P., & Winske, D. (2011, July). Excitation of magnetosonic waves in the terrestrial magnetosphere: Particle-in-cell simulations. *Journal of Geophysical Research (Space Physics)*, *116*, A07212. doi: 10.1029/2010JA016372

Lu, Q., Ke, Y., Wang, X., Liu, K., Gao, X., Chen, L., & Wang, S. (2019, Jun). Two-Dimensional gcPIC Simulation of Rising-Tone Chorus Waves in a Dipole Magnetic Field. *Journal of Geophysical Research (Space Physics)*, *124*(6),

4157-4167. doi: 10.1029/2019JA026586

Ma, Q., Li, W., Bortnik, J., Kletzing, C. A., Kurth, W. S., Hospodarsky, G. B., & Wygant, J. R. (2019). Global Survey and Empirical Model of Fast Magnetosonic Waves Over Their Full Frequency Range in Earth's Inner Magnetosphere. *Journal of Geophysical Research (Space Physics)*, *124*(12), 10270-10282. Retrieved from `https://agupubs.onlinelibrary.wiley.com/doi/abs/10.1029/2019JA027407` doi: 10.1029/2019JA027407

Ma, Q., Li, W., Thorne, R. M., & Angelopoulos, V. (2013, May). Global distribution of equatorial magnetosonic waves observed by THEMIS. *Geophys. Res. Lett.*, *40*, 1895-1901. doi: 10.1002/grl.50434

Meredith, N. P., Horne, R. B., & Anderson, R. R. (2008, June). Survey of magnetosonic waves and proton ring distributions in the Earth's inner magnetosphere. *Journal of Geophysical Research (Space Physics)*, *113*, A06213. doi: 10.1029/2007JA012975

Min, K., Boardsen, S. A., Denton, R. E., & Liu, K. (2018, November). Equatorial Evolution of the Fast Magnetosonic Mode in the Source Region: Observation-Simulation Comparison of the Preferential Propagation Direction. *Journal of Geophysical Research (Space Physics)*, *123*, 9532-9544. doi: 10.1029/2018JA026037

Min, K., & Liu, K. (2016, Jan). Proton velocity ring-driven instabilities in the inner magnetosphere: Linear theory and particle-in-cell simulations. *Journal of Geophysical Research (Space Physics)*, *121*(1), 475-491. doi: 10.1002/2015JA022042

Min, K., & Liu, K. (2020). Linear Instability and Saturation Characteristics of Magnetosonic Waves along the Magnetic Field Line. *Journal of Astronomy and Space Sciences*, *37*, 85-94. Retrieved from `http://janss.kr/journal/article.php?code=73141` doi: https://doi.org/10.5140/JASS.2020.37.2.85

Min, K., Liu, K., Denton, R. E., & Boardsen, S. A. (2018, September). Particle-in-Cell Simulations of the Fast Magnetosonic Mode in a Dipole Magnetic Field: 1-D Along the Radial Direction. *Journal of Geophysical Research (Space Physics)*, *123*, 7424-7440. doi: 10.1029/2018JA025666

Min, K., Liu, K., & Gary, S. P. (2016, Mar). Scalings of Alfvén-cyclotron and ion Bernstein instabilities on temperature anisotropy of a ring-like velocity distribution in the inner magnetosphere. *Journal of Geophysical Research (Space Physics)*, *121*(3), 2185-2193. doi: 10.1002/2015JA022134

Min, K., Liu, K., Wang, X., Chen, L., & Denton, R. E. (2018, January). Fast Magnetosonic Waves Observed by Van Allen Probes: Testing Local Wave Excitation Mechanism. *Journal of Geophysical Research (Space Physics)*, *123*, 497-512. doi: 10.1002/2017JA024867

Min, K., Němec, F., Liu, K., Denton, R. E., & Boardsen, S. A. (2019, Jun). Equatorial Propagation of the Magnetosonic Mode Across the Plasmapause: 2-D PIC Simulations. *Journal of Geophysical Research (Space Physics)*, *124*(6), 4424-4444. doi: 10.1029/2019JA026567

Němec, F., Santolík, O., Gereová, K., Macúšová, E., de Conchy, Y., & Cornilleau-Wehrlin, N. (2005, January). Initial results of a survey of equatorial noise emissions observed by the Cluster spacecraft. *Planetary and Space Science*, *53*, 291-298. doi: 10.1016/j.pss.2004.09.055

Němec, F., Santolík, O., Hrbáčková, Z., & Cornilleau-Wehrlin, N. (2015, March). Intensities and spatiotemporal variability of equatorial noise emissions observed by the Cluster spacecraft. *Journal of Geophysical Research (Space Physics)*, *120*, 1620-1632. doi: 10.1002/2014JA020814

Němec, F., Santolík, O., Pickett, J. S., Hrbáčková, Z., & Cornilleau-Wehrlin, N. (2013, November). Azimuthal directions of equatorial noise propagation determined using 10 years of data from the Cluster spacecraft. *Journal of Geophysical Research (Space Physics)*, *118*, 7160-7169. doi: 10.1002/2013JA019373

933 Němec, F., Santolík, O., Gereová, K., Macúšová, E., Laakso, H., de Conchy, Y., ...
934 Cornilleau-Wehrlin, N. (2006, Jan). Equatorial noise: Statistical study of
935 its localization and the derived number density. *Advances in Space Research*,
936 *37*(3), 610-616. doi: 10.1016/j.asr.2005.03.025
937 Perraut, S., Roux, A., Robert, P., Gendrin, R., Sauvaud, J.-A., Bosqued, J.-
938 M., ... Korth, A. (1982, August). A systematic study of ULF waves
939 above F/H plus/ from GEOS 1 and 2 measurements and their relation-
940 ships with proton ring distributions. *J. Geophys. Res.*, *87*, 6219-6236. doi:
941 10.1029/JA087iA08p06219
942 Posch, J. L., Engebretson, M. J., Olson, C. N., Thaller, S. A., Breneman, A. W.,
943 Wygant, J. R., ... Reeves, G. D. (2015, August). Low-harmonic magnetosonic
944 waves observed by the Van Allen Probes. *Journal of Geophysical Research*
945 *(Space Physics)*, *120*, 6230-6257. doi: 10.1002/2015JA021179
946 Roberts, C. S., & Schulz, M. (1968, Dec). Bounce resonant scattering of particles
947 trapped in the Earth's magnetic field. *J. Geophys. Res.*, *73*(23), 7361-7376.
948 doi: 10.1029/JA073i023p07361
949 Roederer, J. G. (1970). *Dynamics of geomagnetically trapped radiation.* (Physics and
950 Chemistry in Space, Berlin: Springer, 1970)
951 Russell, C. T., Holzer, R. E., & Smith, E. J. (1970). OGO 3 observations of ELF
952 noise in the magnetosphere: 2. The nature of the equatorial noise. *J. Geophys.*
953 *Res.*, *75*, 755. doi: 10.1029/JA075i004p00755
954 Santolík, O., Nemec, F., Gereová, K., Macúšová, E., Conchy, Y., & Cornilleau-
955 Wehrlin, N. (2004, July). Systematic analysis of equatorial noise below
956 the lower hybrid frequency. *Annales Geophysicae*, *22*, 2587-2595. doi:
957 10.5194/angeo-22-2587-2004
958 Santolík, O., Pickett, J. S., Gurnett, D. A., Maksimovic, M., & Cornilleau-Wehrlin,
959 N. (2002, December). Spatiotemporal variability and propagation of equatorial
960 noise observed by Cluster. *Journal of Geophysical Research (Space Physics)*,
961 *107*, 1495. doi: 10.1029/2001JA009159
962 Shklyar, D. R., & Balikhin, M. A. (2017, October). Whistler Mode Waves Be-
963 low Lower Hybrid Resonance Frequency: Generation and Spectral Fea-
964 tures. *Journal of Geophysical Research (Space Physics)*, *122*, 10. doi:
965 10.1002/2017JA024416
966 Shprits, Y. Y. (2009, June). Potential waves for pitch-angle scattering of near-
967 equatorially mirroring energetic electrons due to the violation of the sec-
968 ond adiabatic invariant. *Geophys. Res. Lett.*, *36*, L12106. doi: 10.1029/
969 2009GL038322
970 Sun, J., Gao, X., Lu, Q., Chen, L., Liu, X., Wang, X., ... Wang, S. (2017, May).
971 Spectral properties and associated plasma energization by magnetosonic waves
972 in the Earth's magnetosphere: Particle-in-cell simulations. *Journal of Geophys-*
973 *ical Research (Space Physics)*, *122*, 5377-5390. doi: 10.1002/2017JA024027
974 Tao, X. (2014, May). A numerical study of chorus generation and the related varia-
975 tion of wave intensity using the DAWN code. *Journal of Geophysical Research*
976 *(Space Physics)*, *119*, 3362-3372. doi: 10.1002/2014JA019820
977 Tao, X., & Li, X. (2016, July). Theoretical bounce resonance diffusion coefficient for
978 waves generated near the equatorial plane. *Geophys. Res. Lett.*, *43*, 7389-7397.
979 doi: 10.1002/2016GL070139
980 Thomsen, M. F., Denton, M. H., Gary, S. P., Liu, K., & Min, K. (2017, Dec).
981 Ring/Shell Ion Distributions at Geosynchronous Orbit. *Journal of Geo-*
982 *physical Research (Space Physics)*, *122*(12), 12,055-12,071. doi: 10.1002/
983 2017JA024612
984 Umeda, T., Omura, Y., & Matsumoto, H. (2001, June). An improved mask-
985 ing method for absorbing boundaries in electromagnetic particle simula-
986 tions. *Computer Physics Communications*, *137*, 286-299. doi: 10.1016/
987 S0010-4655(01)00182-5

Walker, S. N., Balikhin, M. A., Shklyar, D. R., Yearby, K. H., Canu, P., Carr, C. M., & Dandouras, I. (2015, Nov). Experimental determination of the dispersion relation of magnetosonic waves. *Journal of Geophysical Research (Space Physics)*, *120*(11), 9632-9650. doi: 10.1002/2015JA021746

Xiao, F., & Feng, X. (2006, May). Modeling Density and Anisotropy of Energetic Electrons Along Magnetic Field Lines. *Plasma Science and Technology*, *8*, 279-284. doi: 10.1088/1009-0630/8/3/07

Yuan, Z., Yao, F., Yu, X., Huang, S., & Ouyang, Z. (2019, May). An Automatic Detection Algorithm Applied to Fast Magnetosonic Waves With Observations of the Van Allen Probes. *Journal of Geophysical Research (Space Physics)*, *124*(5), 3501-3511. doi: 10.1029/2018JA026387

Zhima, Z., Chen, L., Fu, H., Cao, J., Horne, R. B., & Reeves, G. (2015, November). Observations of discrete magnetosonic waves off the magnetic equator. *Geophys. Res. Lett.*, *42*, 9694-9701. doi: 10.1002/2015GL066255

Zou, Z., Zuo, P., Ni, B., Wei, F., Zhao, Z., Cao, X., ... Gu, X. (2019, Jul). Wave Normal Angle Distribution of Fast Magnetosonic Waves: A Survey of Van Allen Probes EMFISIS Observations. *Journal of Geophysical Research (Space Physics)*, *124*(7), 5663-5674. doi: 10.1029/2019JA026556